

Supporting Information

Dual-Source Coevaporation of Low-Bandgap

$\text{FA}_{1-x}\text{Cs}_x\text{Sn}_{1-y}\text{Pb}_y\text{I}_3$ Perovskites

James M. Ball,¹ Leonardo Buizza,¹ Harry C. Sansom,¹ Michael D. Farrar,¹ Matthew T. Klug,¹
Juliane Borchert,¹ Jay Patel,¹ Laura M. Herz,¹ Michael B. Johnston,^{1*} and Henry J. Snaith^{1*}

¹Department of Physics, University of Oxford, Clarendon Laboratory, Parks Road, Oxford, OX1 3PU,
United Kingdom

*Authors to whom correspondence should be addressed: michael.johnston@physics.ox.ac.uk,
henry.snaith@physics.ox.ac.uk

TABLE OF CONTENTS

S1. EXPERIMENTAL METHODS	2
S2. X-RAY DIFFRACTION	7
S3. SCANNING ELECTRON MICROSCOPY	12
S4. UV-VIS-NIR ABSORPTION AND STEADY-STATE PL.....	17
S5. INDUCTIVELY-COUPLED PLASMA MASS SPECTROSCOPY	19
S6. MOBILITY AND DIFFUSION LENGTH CALCULATIONS	20
S7. SPECTRAL MISMATCH FACTOR CALCULATIONS	22
S8. SOLAR CELL CHARACTERISATION	24
S9. THICKNESS MEASUREMENTS	29
S10. ESTIMATION OF BANDGAPS AND LIMITING V_{oc}	29
S11. SOLUTION PROCESSED FILMS AND DEVICES	32
REFERENCES.....	37

S1. EXPERIMENTAL METHODS

Precursor preparation and handling

The precursor mixtures were prepared using CsI (Alfa Aesar, 99.9%, ~20 mesh beads, CAS number 7789-17-5), PbI₂ (Alfa Aesar, 99.999%, ultradry, ~10 mesh beads, CAS number 10101-63-0), SnI₂ (Alfa Aesar, 99.999%, ultradry, ~10 mesh beads, CAS number 10294-70-9), and SnF₂ (Sigma-Aldrich, 99%, CAS number 7783-47-3). All processing and handling of the precursors was within nitrogen-filled gloveboxes (O₂ and H₂O < 20 ppm). To transport materials between gloveboxes they were sealed in glass vials and then vacuum bags to prevent oxygen and moisture ingress. The required mass ratios of precursors were weighed inside a glovebox into a single vial for each SnF₂ ratio. The raw mixtures were ground into powders using a pestle and mortar for ~10 minutes. They were then heated in either alumina or quartz crucibles with loose fitting lids under inert atmosphere at 450°C (above the melting points of PbI₂, SnI₂, and SnF₂) for 2 hours and then allowed to cool naturally to room temperature. When using alumina crucibles the reaction product was scraped out using a clean metal spatula. When using quartz crucibles the ingot could be knocked out by tapping on the base and then coarsely ground in a pestle and mortar.

Perovskite and precursor deposition

Perovskite and precursor thin-films were deposited by vacuum evaporation (Kurt J. Lesker) in a chamber that is attached to nitrogen-filled glovebox (O₂ and H₂O < 1 ppm) so that samples and source materials can be loaded and unloaded under inert conditions. The formamidinium iodide (FAI, Dyesol Ltd., CAS number 879643-71-7) and precursor mixtures were evaporated from alumina crucibles in separate thermal sources at a pressure of ~5×10⁻⁶ mbar. Initially the sources were heated to reach apparent material evaporation rate set points that were detected using dedicated quartz crystal microbalances, one for each source. The apparent rates were set to be identical to previously published work using FAI and PbI₂ in the same evaporation system.³² After a stabilisation period of ~15 minutes, the substrate shutter was opened to allow material deposition onto the substrates for ~10000 s. To maximise the uniformity of the deposition the sample holder was rotated during deposition and its temperature was maintained at 20°C. During perovskite deposition, both sources were evaporating the constituent materials simultaneously, i.e. coevaporation.

Characterisation sample preparation

Thin-film samples for UV-vis-NIR absorption, PL, XRD, THz photoconductivity, and thickness measurements were prepared on quartz substrates that were cleaned sequentially in acetone (Sigma-Aldrich, 99%, CAS number 67-64-1) and isopropanol (IPA, Sigma-Aldrich, 99.5%, CAS number 67-63-0) under ultrasonic agitation (Grant XUBA3) for 10 minutes, followed by 5 minutes exposure to O₂ plasma (Diener Pico). Perovskite and precursor samples were deposited by coevaporation and single-source evaporation, respectively.

Device sample preparation

Devices were fabricated on indium tin oxide (ITO)-coated glass substrates (Shenzhen Huayu Union Technology Co Ltd, $10 \Omega/\square$) that were rinsed sequentially in dilute detergent (Hellmanex III, 1 % by volume in deionised water), deionised (DI) water (Milli-Q Direct 8), acetone, and IPA, dried in a stream of N_2 , and exposed to O_2 plasma for 5 minutes. The hole-transport layer was deposited by spincoating a dilution of 1 part poly(3,4-ethylenedioxythiophene) polystyrene sulfonate (PEDOT:PSS, Heraeus Clevis P VP.AI4083) in 2 parts methanol (Sigma-Aldrich, 99.8%, CAS number 67-56-1) after filtering with a $0.45 \mu\text{m}$ glass microfiber (GMF) filter. Spincoating was carried out in air (speed = 4000 rpm, acceleration = 4000 rpm/s, time = 40 s), followed by annealing at 150°C on a hotplate for 10 minutes. The substrates were then quickly transferred to a nitrogen-filled glovebox for perovskite deposition by coevaporation. The electron-transport layer comprised two sub-layers: phenyl- C_{61} -butyric acid methyl ester (PCBM, Solenne BV, 99.5%) and bathocuproine (BCP, Sigma-Aldrich, 99.99%, 4733-39-5), that were both deposited by spin coating in a nitrogen-filled glovebox. PCBM was dissolved in a mixture of chlorobenzene (CB, Sigma-Aldrich, 99.8%, anhydrous, CAS number 108-90-7) and 1,2-dichlorobenzene (DCB, Sigma-Aldrich, 99%, anhydrous, CAS number 95-50-1) at a concentration of 20 mg/ml with a ratio of 3:1 CB:DCB, heated to 90°C for 10 minutes, filtered with a $0.2 \mu\text{m}$ polytetrafluoroethylene (PTFE) filter, returned to the hotplate at 90°C , and spincoated hot at speed = 2000 rpm, acceleration = 1000 rpm/s, time = 30 s. After PCBM spincoating, the samples were dried at 90°C on a hotplate for 2 minutes. BCP was dissolved in IPA (Sigma-Aldrich, anhydrous, 99.5%, CAS number 67-63-0) at 0.5 mg/ml and stirred overnight, filtered with a $0.45 \mu\text{m}$ PTFE filter, and spincoated on top of the PCBM layer at speed = 4000 rpm, acceleration = 1000 rpm/s, time = 20 s. The samples were then transferred through air into a metal evaporator (Kurt J. Lesker, Nano36) for top Ag electrode deposition through a shadow mask up to 100 nm thickness under a pressure of $\sim 10^{-6}$ Torr.

Current density-voltage characterisation

J-V characterisation was performed in air using a Keithley 2400 sourcemeter and simulated air-mass 1.5 global tilt (AM1.5G) solar irradiation with either an ABET Technologies Sun 2000 (filtered Xe lamp) or a Wavelabs Sinus-220 (light-emitting diode array) solar simulator. The intensity of the ABET simulator was calibrated with a certified Si reference cell with a BK7 glass window (PV Measurements) and an additional KG2 filter (Thorlabs, NENIR206B; certified with the filter at Centre for Renewable Energy Systems Technology, Loughborough University). The intensity of the Wavelabs simulator was calibrated with a certified Si reference cell with a KG3 window (Fraunhofer ISE). To calculate the spectral mismatch factors the emission spectrum of the ABET simulator was measured using a spectrograph (Ocean Optics MAYA 2000Pro) that was spectrally calibrated with a certified quartz-tungsten-halogen lamp (Ocean Optics HL-3P-CAL) and the emission spectrum of the Wavelabs simulator was measured using its internal spectrograph. The spectral mismatch factor for

both lamps was calculated using a standard procedure⁴⁰ based on the lamp spectra and measured external quantum efficiency (EQE) data (see below, Section S7) and used to correct the measured power conversion efficiencies. The spectral mismatch factor was usually within +/- 2% compared to AM1.5G (except for the sample with $\mu=1$) implying that the measured values of J_{sc} for different cells were measured under comparable conditions, close to 100 mW/cm². A more detailed discussion of the solar simulator calibration method and spectral mismatch calculations is given in Section S7. The areas of the pixels were defined using black anodised aluminium shadow masks placed directly in contact with glass side of the substrate within an enclosed sample holder.

External quantum efficiency measurements

External quantum efficiency measurements were performed using a custom-built system. The monochromatic illumination source was provided using a 250 W halogen lamp and monochromator (Princeton Instruments Acton SP2150, with FA2448 filter wheel), which was chopped (Thorlabs MC2000B-EC) at 280 Hz and focused to a spot size on the sample that was smaller than the pixel defined by the evaporated rear electrode. Two series-connected white LEDs (Luxeon Star/O LXHL-NWE8) driven at $I = 0.1$ A, $V = 7.2$ V (TTi QL564P) were focused onto the sample to provide a background white-bias. The pixel was selected using a multiplexor (National Instruments NI SCXI-1331 multiplexor within an NI SCXI-1000 chassis), and its AC current signal due to the chopped monochromatic illumination was converted to a voltage using a 50 Ω resistor. The amplitude of this voltage signal was measured using a lock-in amplifier (Stanford Research Systems SR830). The absolute value of EQE was calculated based on the ratio of this voltage signal to that of a signal generated by a reference Si photodiode of known EQE calibrated against a Thorlabs FDS100-CAL Si photodiode.

X-ray diffraction

XRD measurements were performed using the $K\alpha_1$ wavelength of a Cu x-ray source in a Panalytical X'pert Pro. Samples were mounted in holders with domed plastic lids and a rubber o-ring in a N₂-filled glovebox to prevent O₂ and moisture ingress during measurements in air. Precursors were ground into powders using a pestle and mortar for ~10 minutes for powder diffraction measurements. Thin-films were deposited on quartz substrates. Pawley fittings were used to assign the unit cells of known materials to the collected XRD patterns using Topas-5 software.

Thickness measurements

Perovskite film thicknesses were measured using a Veeco Dektak 150 surface profilometer. The thickness was defined at the step height across a scratch made in the film using a razor blade on a quartz substrate.

Inductively-coupled plasma mass spectroscopy

ICP-MS was performed at the Materials Innovation Factory, University of Liverpool. The instrument was a PerkinElmer NexION 2000 with a PerkinElmer s10 auto sampler and used Syngistix control and analysis software. The measurements were performed with an RF power of 1200 W, nebuliser gas flow of 0.5 L/min, Argon plasma, auxiliary gas flow of 1.2 L/min, and plasma gas flow = 15 L/min. The instrument was calibrated with an ^{127}In internal standard for measuring ^{118}Sn and ^{133}Cs , and a ^{209}Bi internal standard for measuring ^{208}Pb . Each measurement consisted of 3 readings per sample and each reading consisted of 20 sweeps over the mass range of interest. The relative standard deviation of the measurement (RSD) was calculated from the 3 readings per sample. The samples were prepared by dissolving one evaporated thin-film of perovskite on a quartz glass substrate (13 mm diameter) per SnF_2 fraction, u , in 10 ml of aqueous HCl (Alfa Aesar, 36.5%, 99.999% purity, CAS 7647-01-0) for 30 minutes at room temperature. Three solutions for each value of u were prepared by diluting 82.6 μL of the concentrated stock solutions in 9.92 ml of DI water (Milli-Q Direct 8). Reference solutions were prepared using an identical procedure but with a blank quartz substrate.

Thin-film UV-Vis-NIR absorption

Transmittance and reflectance spectra were used to calculate the optical density of thin-films using a Bruker Vertex 80v Fourier-Transform Infrared (FTIR) spectrometer with a tungsten halogen light source and a silicon diode detector. Samples were vacuum-sealed in a N_2 -filled glovebox before transportation to the instrument where they were exposed to air for approximately 30 s while being transferred into the sample compartment. The sample compartment was then pumped down to a vacuum of 2.72 mbar in ~ 120 s. Samples were illuminated from the film side and measured in both transmission and reflection mode. The 100% reflection (R_{100}) and 0% transmission (T_0) reference measurements were taken using a protected silver mirror (Thorlabs, PF10-03-P01, reflects $\sim 100\%$ of incident light in the region of interest) in place of the sample, and the 0% reflection (R_0) and 100% transmission (T_{100}) reference measurements were taken with no sample. Reference reflectance data for the mirror provided by the manufacturer, R_{ref} , was also used in the correction. The absorbance was calculated as $A = -\ln(T/(1 - R))$ where $T = (T_{sample} - T_0)/(T_{100} - T_0)$ and $R = R_{ref}(R_{sample} - R_0)/(R_{100} - R_0)$, which are the sample transmittance and reflectance values after correcting the T_{sample} and R_{sample} measurements for optical dispersion with the aforementioned reference measurements. The absorption coefficients were then calculated as $\alpha = A/d$, where d is the sample thickness.

Device reflectance

The reflectance of a complete solar cell device illuminated through the glass side was measured in air using a bifurcated optical fibre (Ocean Optics QR600-7-SR125BX) with one arm transmitting light from the source (Ocean Optics DH-2000-BAL) onto the sample and the other arm directing the reflected light from the sample into a spectrograph (Ocean Optics MAYA 2000Pro). The measured

spectrum was corrected using reference measurements of a protected silver mirror (Thorlabs, PF10-03-P01) or no sample. Reference reflectance data for the mirror provided by the manufacturer, R_{ref} , was also used in the correction. The device reflectance was thus calculated as

$R = R_{ref}(R_{sample} - R_0)/(R_{100} - R_0)$. The proportion of incident light absorbed by the cell was estimated as $1 - R$.

Steady-state photoluminescence

Photoluminescence (PL) spectra were measured following excitation by a 400 nm continuous wave laser with a power density of 1.27 W/cm² (Picoquant, LDH-D-C-405M). The PL emitted was collected and coupled into a grating spectrometer (Princeton Instruments SP-2558), after which light was detected by an iCCD camera (PI-MAX4, Princeton Instruments). Measurements were carried out in vacuum.

Time-resolved photoluminescence

TRPL transients were measured by time-correlated single photon counting. The same laser as above was used to photoexcite the thin films from the side of the perovskite film, but under pulsed excitation mode. A repetition rate of 5 MHz was used for all measurements, at fluences of 53 and 420 nJ/cm². PL was collected using the same monochromator, with a photon-counting detector (PDM series from MPD). Timing is controlled electronically using a PicoHarp300 event timer. PL decays were measured as a function of time, t , at the initial peak wavelengths. Measurements were carried out in vacuum. The low-fluence emission intensity, $I (=I_0$ at $t=0$), decays were fitted with a stretched exponential between 0-190 ns:

$$I = I_0 \exp\left(-\left(\frac{t}{\tau_{avg}}\right)^\beta\right)$$

where τ_{avg} is the effective lifetime and β is the exponential stretching parameter.

THz photoconductivity

An amplified laser system (Spectra Physics, MaiTai – Ascend – Spitfire), with a 5 kHz repetition rate, centre wavelength of 800 nm, and pulse duration of 35 fs was used to generate THz radiation via the inverse-spin Hall effect from an emitter made of 2 nm of tungsten / 1.8 nm of Co₄₀Fe₄₀B₂₀ / 2 nm of platinum, supported by a quartz substrate. The THz probe was focused onto the sample and detected via free-space electro-optical sampling in a ZnTe(110) crystal of thickness 200 μ m. Samples were excited using 800 nm pulsed excitation. Mobilities were calculated from the initial transmitted signal at time = 0 ps at fluences of 6.8, 14.2, and 29.4 μ J/cm². Measurements were carried out under low vacuum ($< 10^{-2}$ mbar). Further details of the mobility and diffusion length calculations based on these measurements are given in Section S6.

S2. X-RAY DIFFRACTION

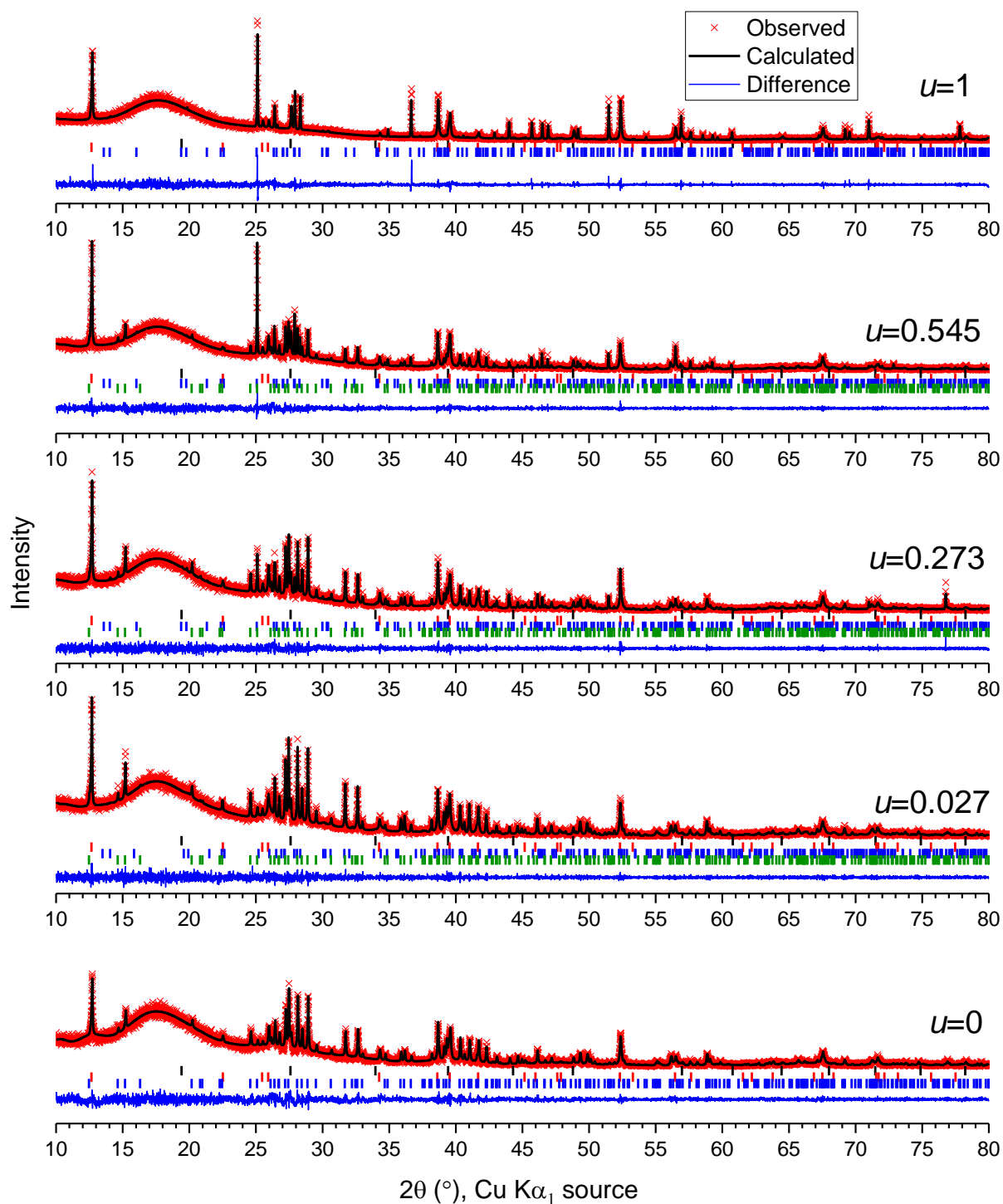


Figure S1. Pawley fits to powder XRD patterns of melted precursor mixtures with different SnF_2 fractions, u , after grinding but before melting. Black, red, blue, and green tick marks indicate peak positions for CsI , PbI_2 , SnF_2 , and SnI_2 , respectively.

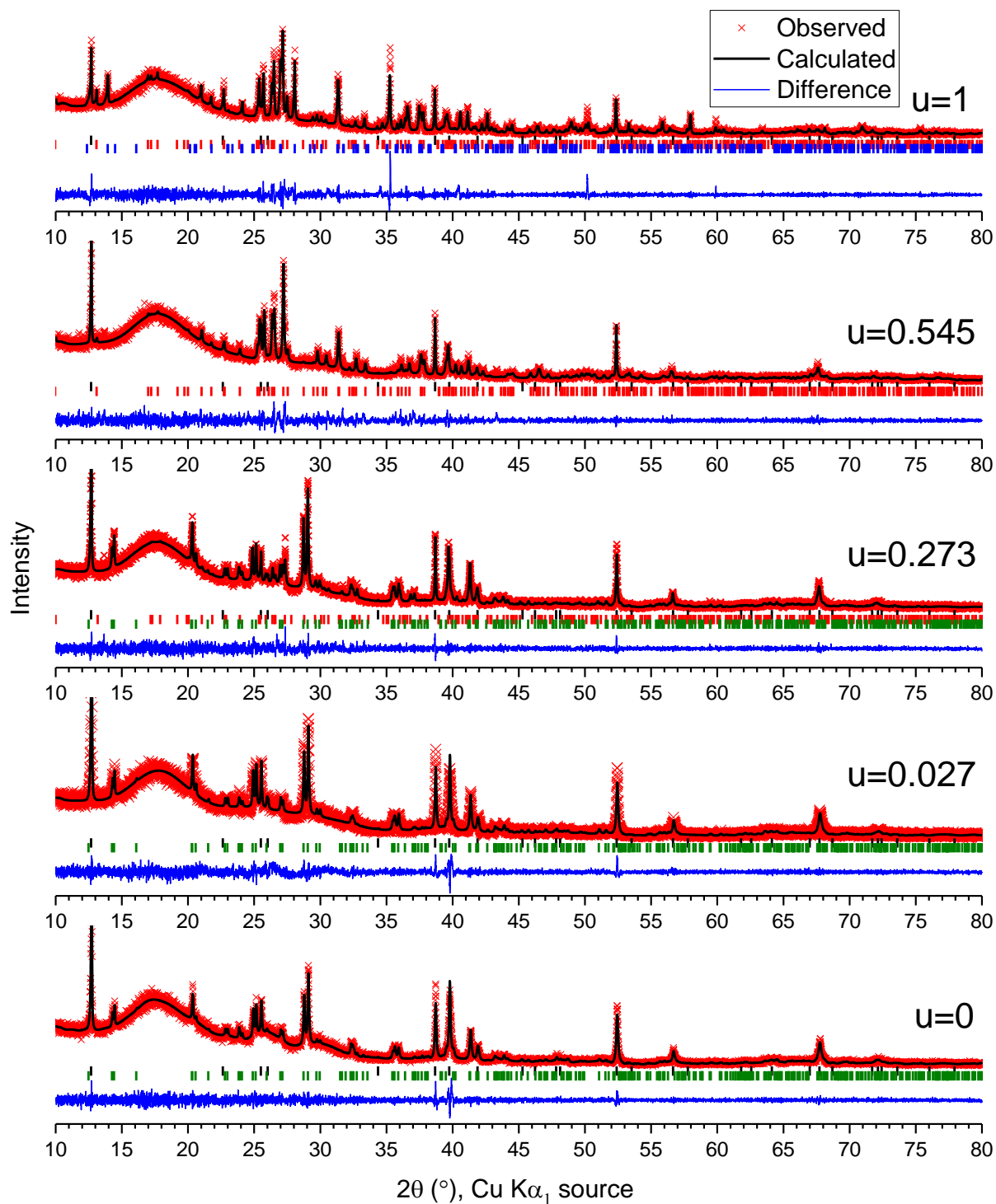


Figure S2. Pawley fits to powder XRD patterns of melted precursor mixtures with different SnF_2 fractions, u , after melting and grinding. Black, red, blue, and green tick marks indicate peak positions for PbI_2 , $\delta\text{-CsSnI}_3$ (1D non-perovskite yellow phase, space group $Pnma$), an unidentified phase, and $\gamma\text{-CsSnI}_3$ (3D perovskite black phase, space group $Pnam$), respectively.

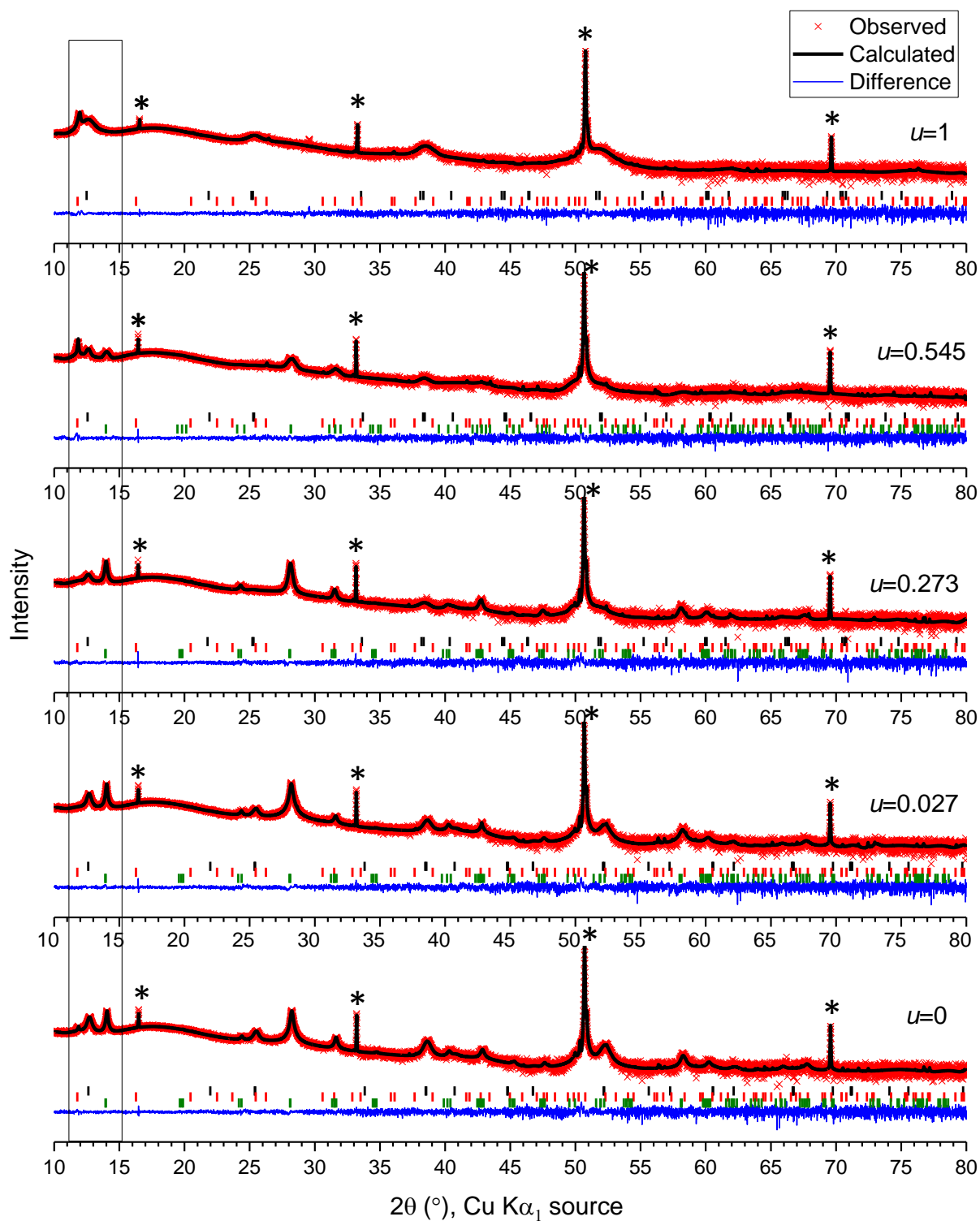


Figure S3. Pawley fits to XRD patterns of evaporated perovskite thin-films made with different SnF_2 fractions, u . Black, red, and green tick marks indicate peak positions for PbI_2 , $\delta\text{-FAPbI}_3$ (1D non-perovskite yellow phase, space group P63mc), and FASnI_3 (3D perovskite black phase, space group Amm2) respectively.

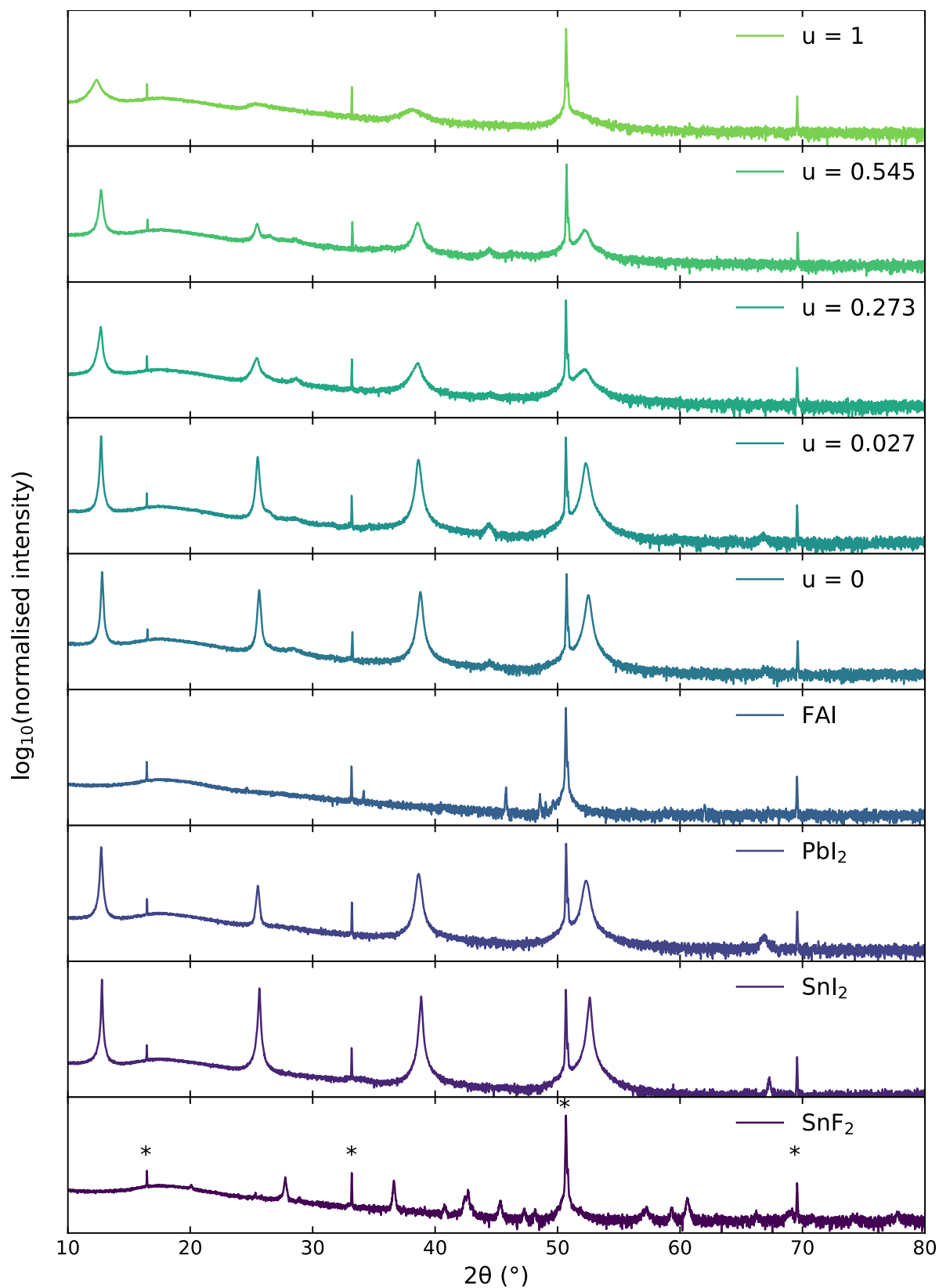


Figure S4. XRD spectra of evaporated thin-films of precursors, including mixtures for different SnF_2 ratios, u , compared to individual precursors, on quartz substrates normalised to the most intense peak. Peaks corresponding to the z-cut quartz substrates are highlighted with asterisks for SnF_2 . The 2θ angle corresponds to the $\text{K}\alpha_1$ wavelength of the Cu x-ray source.

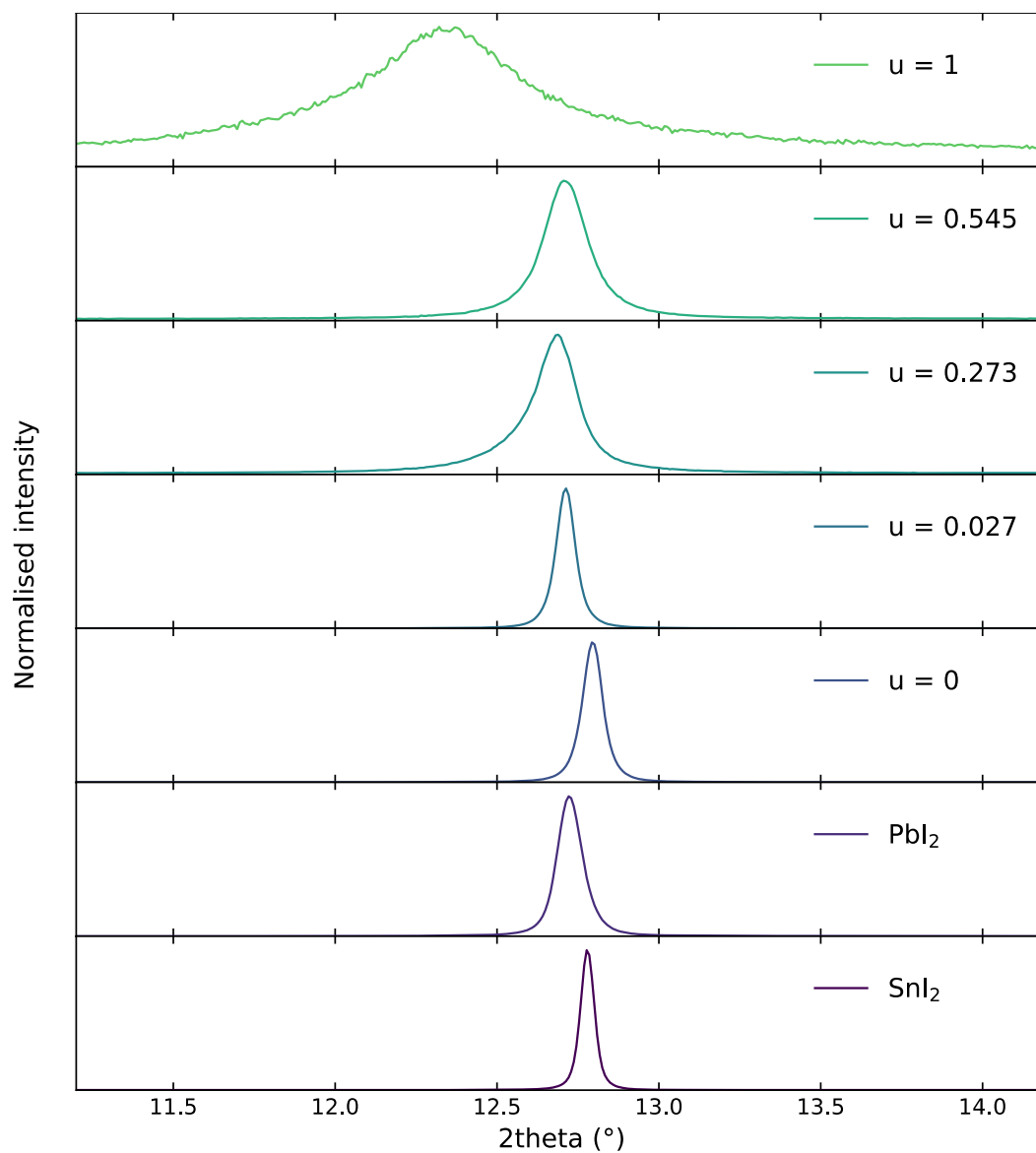


Figure S5. XRD spectra of evaporated thin-films of precursors on quartz substrates, with different SnF_2 fractions, u , normalised to the most intense non-quartz peak, highlighting the main low-angle peak.

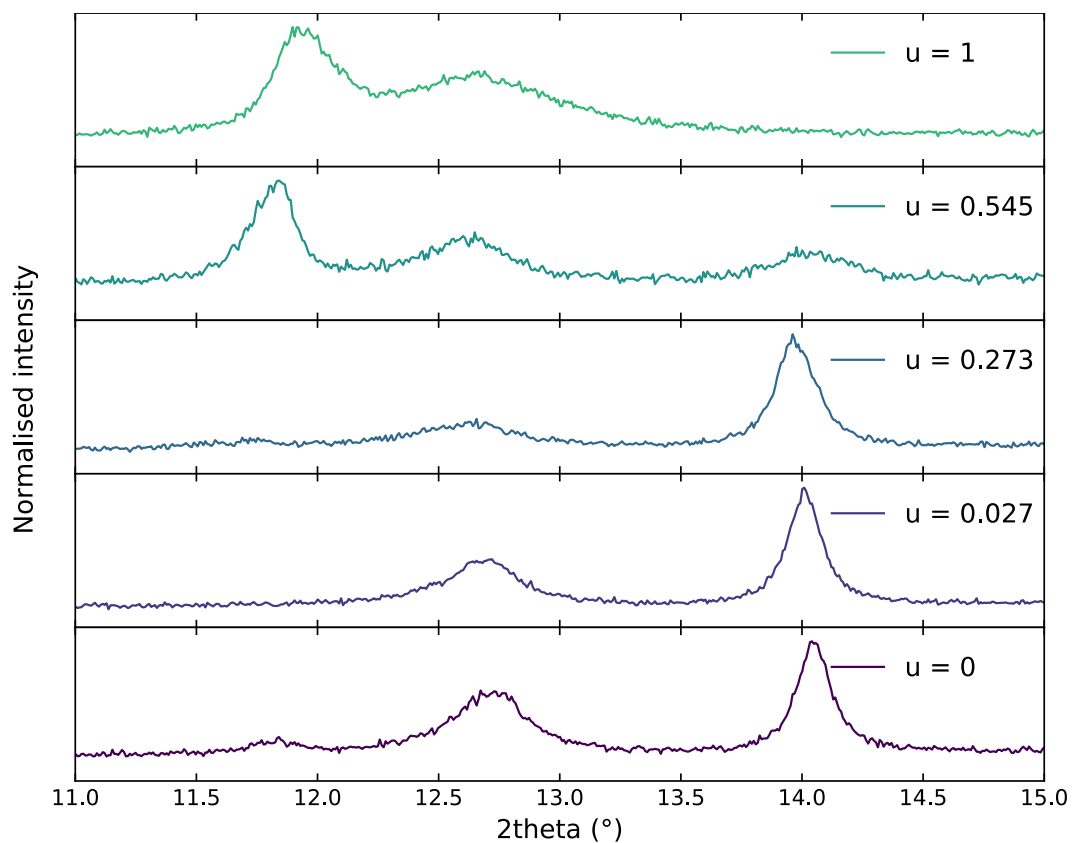


Figure S6. XRD spectra of evaporated perovskite thin-films on quartz substrates normalised to the most intense non-quartz peak, highlighting the main low-angle peaks.

S3. SCANNING ELECTRON MICROSCOPY

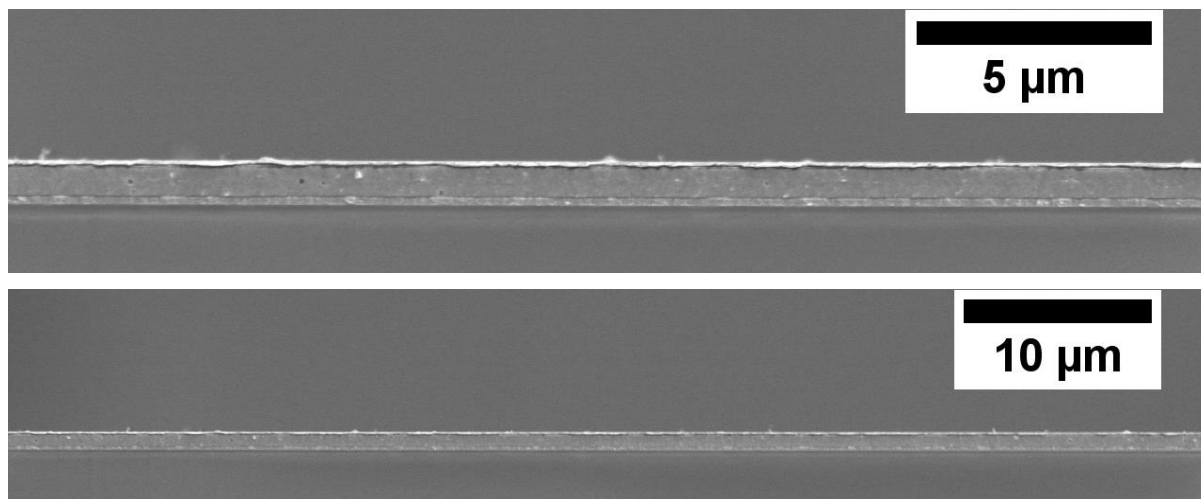


Figure S7. SEM images of the cross-section of a device made with the SnF_2 fraction $u = 0.273$ on two length scales, indicated by the scale bars, highlighting relatively long-range thickness uniformity. From bottom to top, the layers seen in image are: glass, ITO, PEDOT:PSS, perovskite, PCBM/BCP, Ag, and vacuum, as highlighted in main text Figure 3a.

The perovskite grain sizes within the evaporated thin-films were estimated from image analysis of top-view SEM images. The images, shown in Figures S8a-13a, were taken on complete devices, including the electron-transport layer, but in regions outside of the evaporated top electrode. The analyses were performed using the Fiji distribution¹ of ImageJ v1.52n.² The following steps were used in the processing of each image: 1. Define the scale by measuring the number of pixels spanned by the embedded scale bar from the instrument; 2. Crop to 2559 x 1710 pixels to remove metadata embedded in the image; 3. Apply “Enhance contrast” function using histogram equalisation with “Saturated pixels” set to 0.3%; 4. Apply “Find maxima” function with Prominence set to > 25 (except for samples with $u=0.018$ and 0.091 , where Prominence was set to >5), with “Strict” selected; 5. Apply “Analyse particles” function, excluding edges, which generates an image of particle boundaries and a list of particle areas; 6. Overlay the image of particle boundaries on the original, shown in Figures S8b-13b; 7. Add scale bars to the images; 8. Further crop into a square image. Histograms of the grain size distribution (Figures S8c-13c) were generated using the list of areas generated in step 5. with the approximation that that grains are circular. The grain sizes are thus given as a pseudo-diameter: the diameter of the approximated circles of known area.

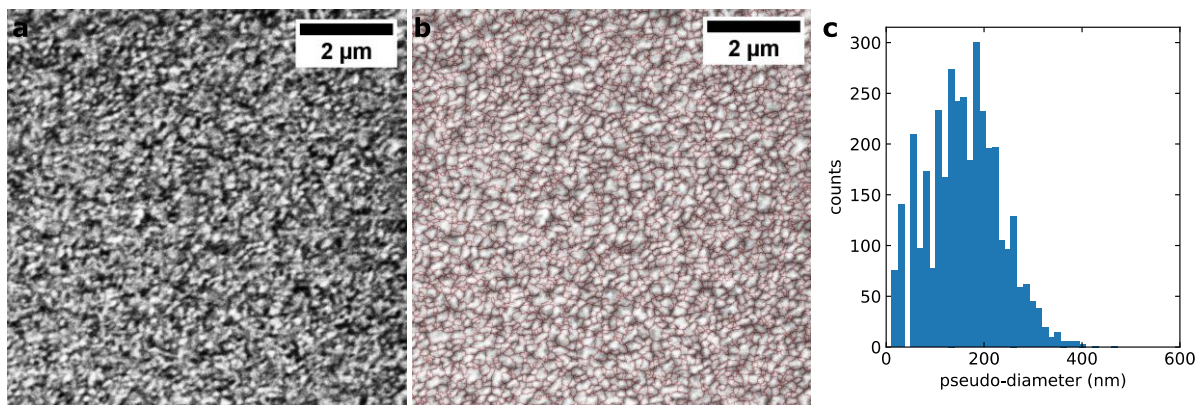


Figure S8. Scanning electron microscopy images of perovskite films for the SnF_2 fraction $u = 0$: (a) top view (equalised histogram with nearest neighbour median filter), (b) the same top-view with segmented overlay based on positions of local maxima used for estimation of the distribution of grain sizes, (c) histogram of grain pseudo-diameters where grains are approximated as circles of areas given by the segmentation map.

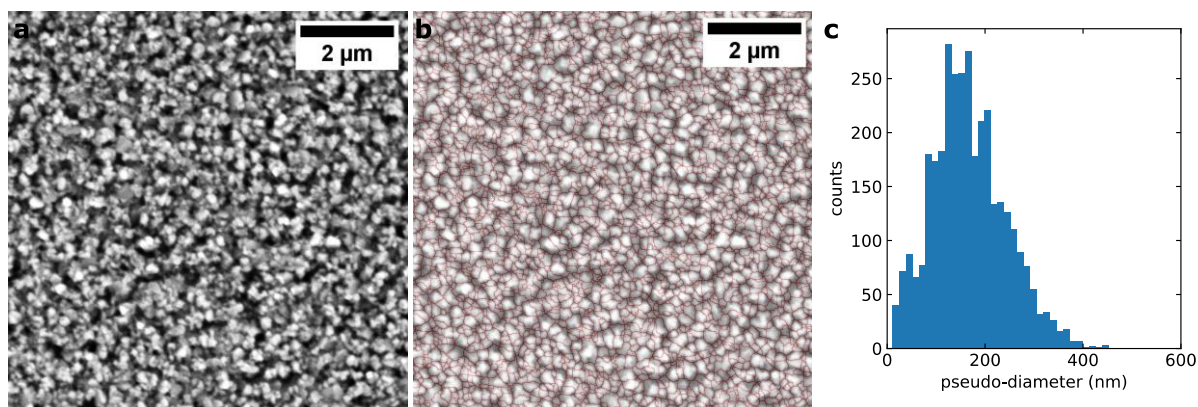


Figure S9. Scanning electron microscopy images of perovskite films for the SnF_2 fraction $u = 0.018$: (a) top view (equalised histogram with nearest neighbour median filter), (b) the same top-view with segmented overlay based on positions of local maxima used for estimation of the distribution of grain sizes, (c) histogram of grain pseudo-diameters where grains are approximated as circles of areas given by the segmentation map.

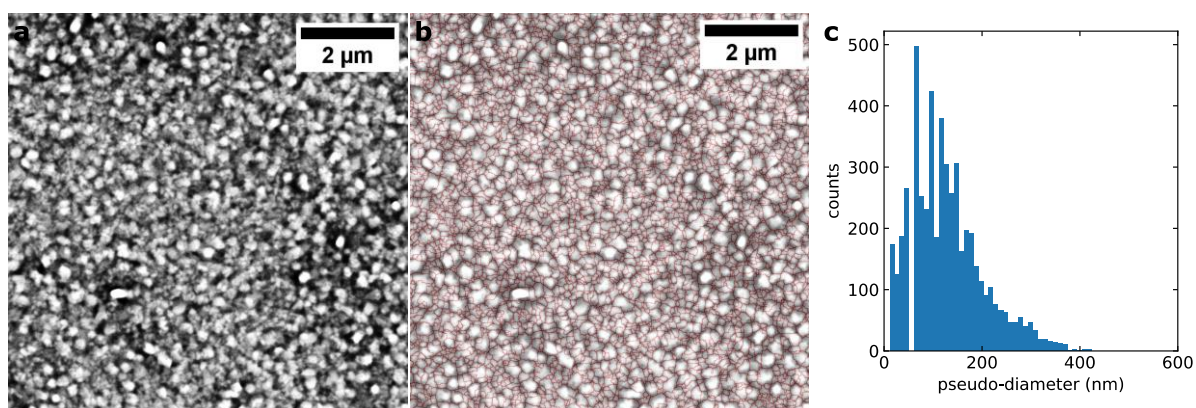


Figure S10. Scanning electron microscopy images of perovskite films for the SnF_2 fraction $u = 0.091$: (a) top view (equalised histogram with nearest neighbour median filter), (b) the same top-view with segmented overlay based on positions of local maxima used for estimation of the distribution of grain sizes, (c) histogram of grain pseudo-diameters where grains are approximated as circles of areas given by the segmentation map.

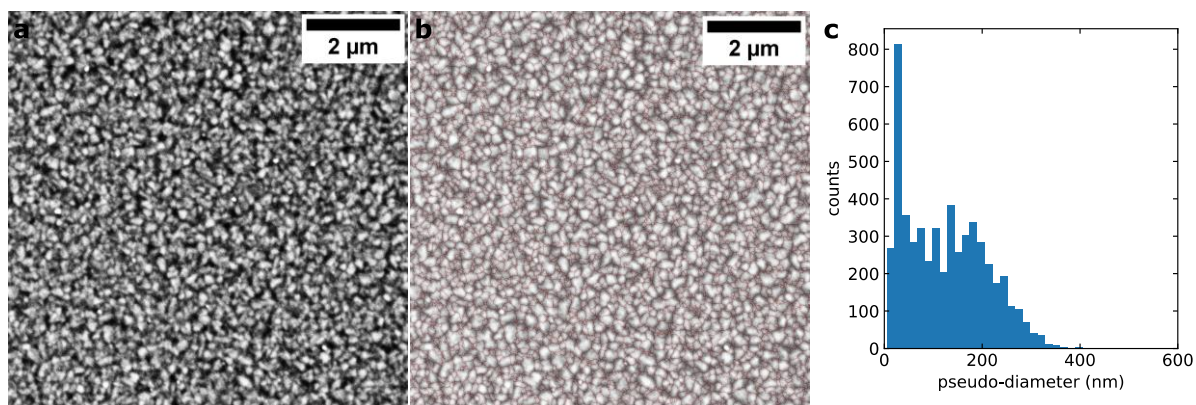


Figure S11. Scanning electron microscopy images of perovskite films for the SnF_2 fraction $u = 0.273$: (a) top view (equalised histogram with nearest neighbour median filter), (b) the same top-view with segmented overlay based on positions of local maxima used for estimation of the distribution of grain sizes, (c) histogram of grain pseudo-diameters where grains are approximated as circles of areas given by the segmentation map.

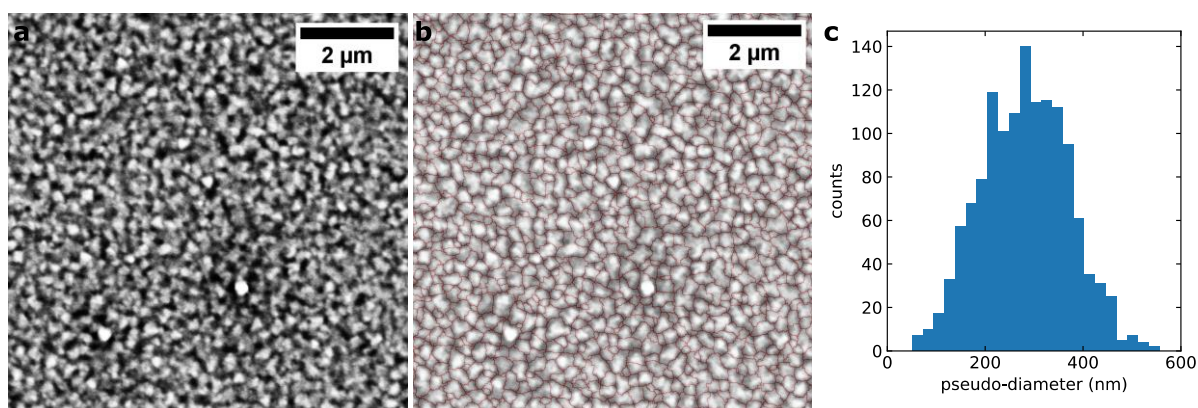


Figure S12. Scanning electron microscopy images of perovskite films for the SnF_2 fraction $u = 0.454$: (a) top view (equalised histogram with nearest neighbour median filter), (b) the same top-view with segmented overlay based on positions of local maxima used for estimation of the distribution of grain sizes, (c) histogram of grain pseudo-diameters where grains are approximated as circles of areas given by the segmentation map.

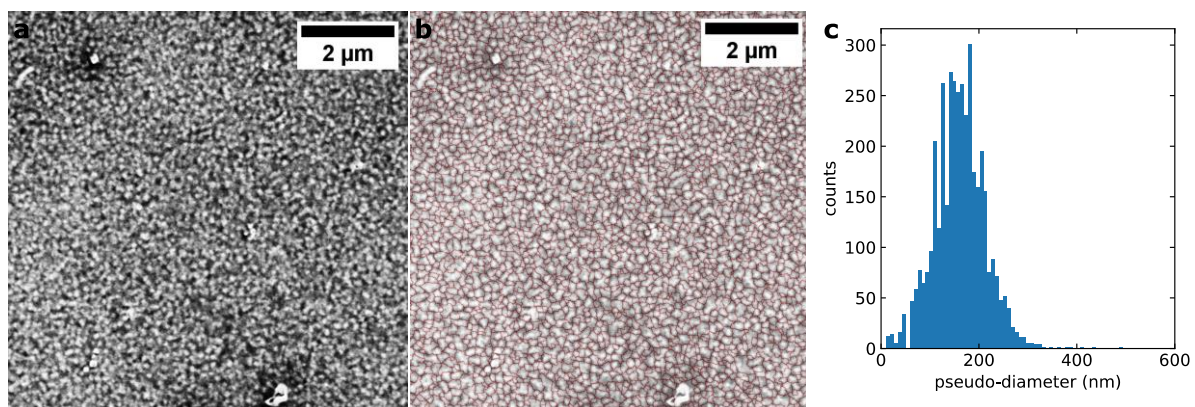


Figure S13. Scanning electron microscopy images of perovskite films for the SnF_2 fraction $u = 1$: (a) top view (equalised histogram with nearest neighbour median filter), (b) the same top-view with segmented overlay based on positions of local maxima used for estimation of the distribution of grain sizes, (c) histogram of grain pseudo-diameters where grains are approximated as circles of areas given by the segmentation map.

S4. UV-VIS-NIR ABSORPTION AND STEADY-STATE PL

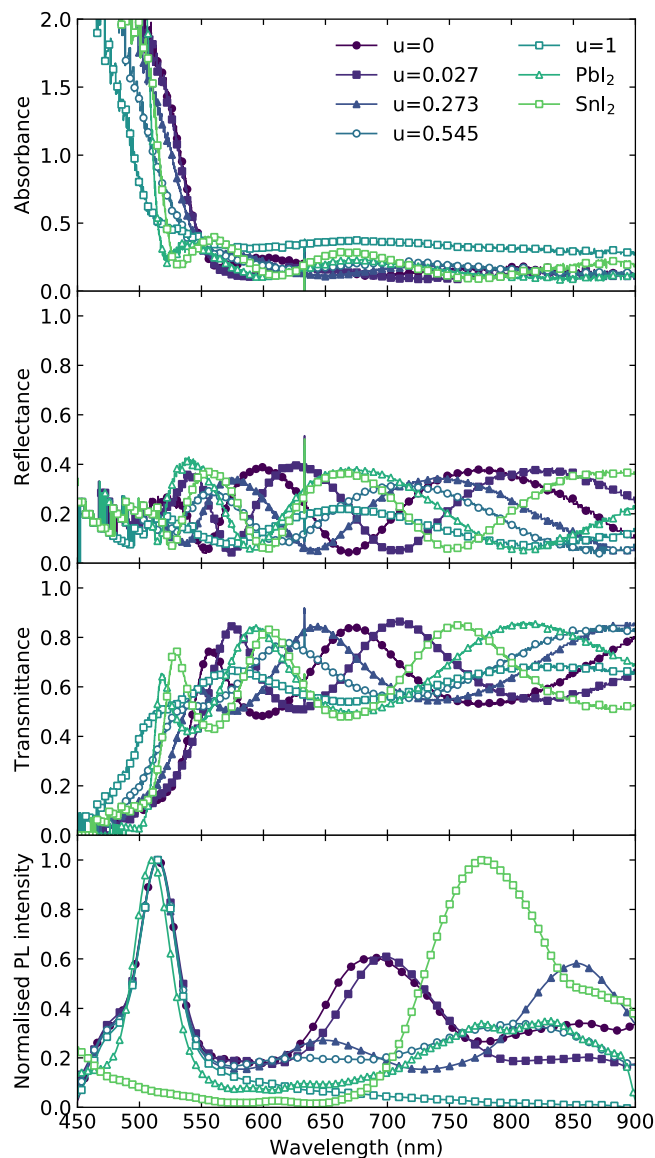


Figure S14. UV-vis-NIR absorption (top) and steady-state PL (bottom) spectra of precursor thin-films on quartz substrates formed by evaporation of melted precursor mixtures. The numbers in the legend correspond to values of u . Markers in the absorption spectra indicate every 75th data point, whereas markers in the PL spectra indicate every 10th data point for mixtures and every 5th data point for single-metal halide references. Absorbance is calculated as $A = -\ln(T/(1 - R))$.

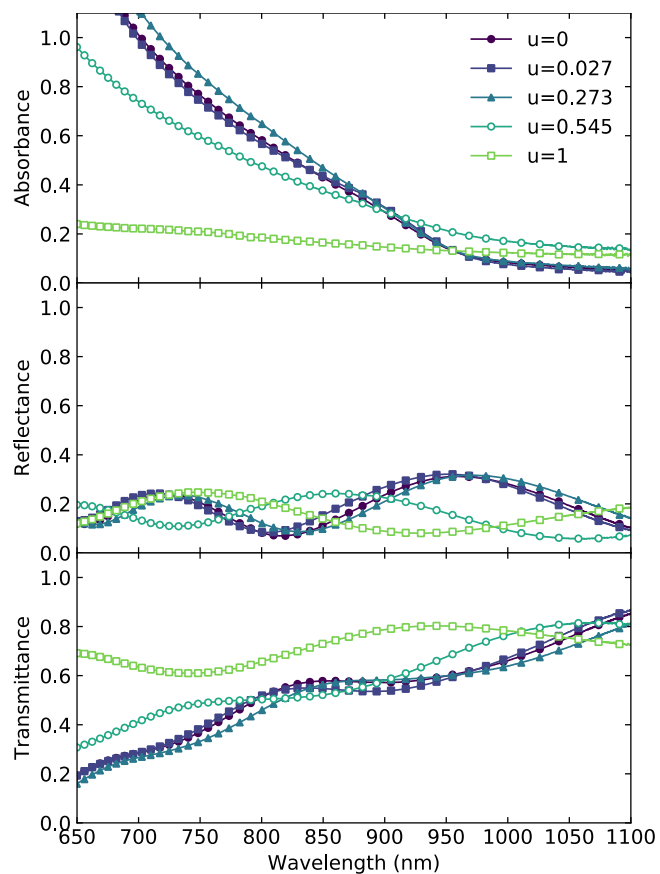


Figure S15. UV-vis-NIR absorbance, reflectance, and transmittance spectra of perovskite thin-films on quartz substrates formed by evaporation. The numbers in the legend correspond to values of the SnF_2 fraction in the precursor, u . Markers in indicate every 75th data point. Absorbance is calculated as $A = -\ln(T/(1 - R))$.

S5. INDUCTIVELY-COUPLED PLASMA MASS SPECTROSCOPY

Table S1. Summary of ICP-MS of elemental concentrations in solutions in parts per billion (ppb) including relative standard deviations (RSD) for different values of u .

u	Sample	^{118}Sn		^{133}Cs		^{208}Pb	
		Conc. (ppb)	RSD (%)	Conc. (ppb)	RSD (%)	Conc. (ppb)	RSD (%)
0	1	237.800	1.2	6.987	0.7	15.426	1.9
	2	248.880	1.6	7.173	2.3	16.724	0.8
	3	242.361	0.5	7.123	1.9	15.481	0.5
0.027	1	274.056	6.3	3.630	6.1	26.127	7.1
	2	293.929	3.2	3.800	2.7	15.838	2.2
	3	271.448	1.9	3.860	1.1	16.344	1.8
0.273	1	277.380	1.9	6.894	1.0	15.757	0.8
	2	283.346	1.7	6.942	3.2	16.354	0.8
	3	272.362	5.3	6.916	4.5	15.675	3.9
0.545	1	252.947	13.3	17.242	12.2	19.342	12.7
	2	250.879	1.5	17.083	0.7	19.118	1.6
	3	250.222	2.9	17.148	1.0	19.489	0.9
1	1	305.940	1.9	27.847	1.2	18.637	4.2
	2	319.802	6.4	28.841	5.3	19.018	5.7
	3	327.619	2.0	29.838	2.0	19.625	2.0

The relative stoichiometries of Sn:Pb and Cs:B-site can be calculated from the concentrations in ppb given in Table S1. The atomic concentration in ppb is equivalent to the dilution concentration in $\mu\text{g/L}$. Dividing the dilution concentration by the atomic mass gives the concentrations in mol/L. The ratios of the molar concentrations can then be used to get the relative stoichiometry. The mean relative stoichiometries are given in Table S1 assuming the perovskite compositions are given by $\text{FA}_{1-x}\text{Cs}_x\text{Sn}_{1-y}\text{Pb}_y\text{I}_3$.

Table S2. Summary of estimates of mean relative stoichiometries inferred from ICP-MS measurements for different values of the SnF₂ fraction, u , assuming the final perovskite composition is given by FA_{1-x}Cs_xSn_{1-y}Pb_yI₃.

u	x	y
0	0.025	0.036
0.027	0.012	0.038
0.273	0.021	0.032
0.545	0.058	0.042
1	0.078	0.033

S6. MOBILITY AND DIFFUSION LENGTH CALCULATIONS

At low fluences ($< 50 \mu\text{Jcm}^{-2}$) there is a linear relationship between the charge-carrier mobility (μ) and the change in photoconductivity of the sample ΔS :

$$\mu = \frac{\Delta S A_{eff}}{Ne} \quad (\text{S1})$$

where A_{eff} is the effective overlap of the optical pump and THz probe beams, N is number of photoexcited charge carriers, and e is the charge of the electron. The change in photoconductivity can in turn be related to the fractional change in terahertz transmission ($\Delta T/T$) using a standard formula for thin-film samples³:

$$\Delta S = -\epsilon_0 c (n_A + n_B) \left(\frac{\Delta T(t=0)}{T} \right) \quad (\text{S2})$$

where ϵ_0 is the vacuum permittivity, c is the speed of light, and n_A and n_B are the refractive indices of vacuum and the z-cut quartz substrate, respectively. We can calculate N using:

$$N = \phi \frac{E \lambda}{h c} (1 - R_{pump}(\lambda)) (1 - T_{pump}(\lambda)) \quad (\text{S3})$$

where ϕ branching ratio of photons to free charges, E is the electric field, λ is the pump wavelength, h is Planck's constant, R_{pump} is the pump reflectance, and T_{pump} is the pump transmittance. By combining equations S3, S2 and S1, we can thus calculate the effective charge-carrier mobility as:

$$\phi \mu = -\epsilon_0 c (n_A + n_B) \frac{A_{eff} h c}{E e \lambda (1 - R_{pump}(\lambda)) (1 - T_{pump}(\lambda))} \left(\frac{\Delta T(t=0)}{T} \right) \quad (\text{S4})$$

Given that the branching ratio $0 \leq \phi \leq 1$, the calculated effective charge-carrier mobility is always an underestimate; only in the case of full conversion of photons to free charges does our value reflect the true mobility. In addition, our calculated value of μ arises from changes in photoconductivity due to both electrons and holes, meaning we calculate an overall sum mobility.

Given the high monomolecular recombination rates, the charge-carrier density under AM1.5G is likely to be well below 10^{15} cm^{-3} .⁴ We thus calculate the diffusion length (L_D), approximating the overall recombination rate simply using the monomolecular recombination rate constant (k_1):

$$L_D = \left(\frac{\mu k_B T}{e k_1} \right)^{\frac{1}{2}} = \left(\frac{2\mu k_B T \tau_{avg}}{e} \right)^{\frac{1}{2}} \quad (\text{S5})$$

where k_B is Boltzmann's constant and T is temperature.

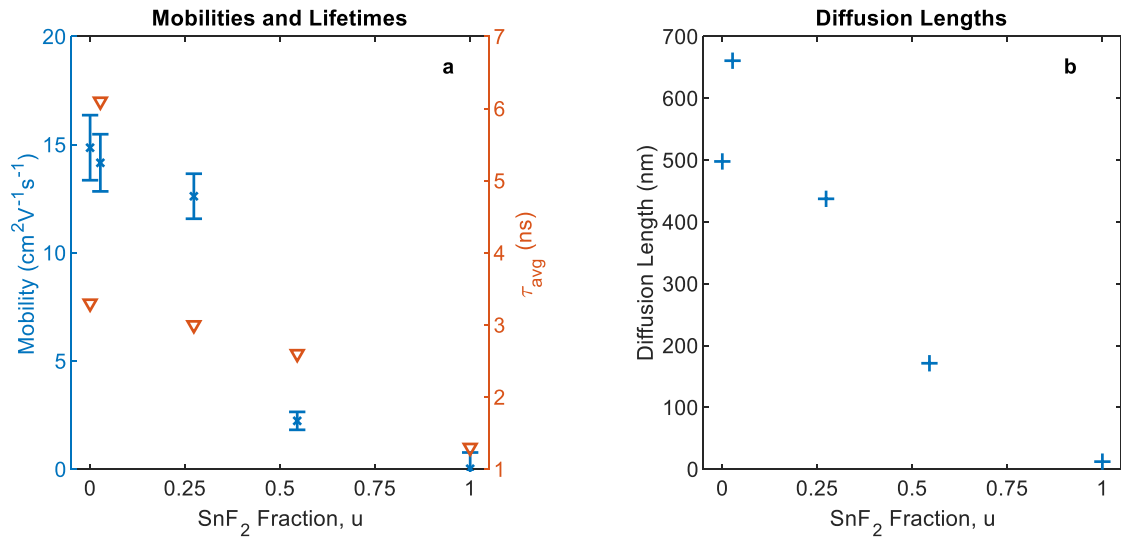


Figure S16. (a) Charge carrier mobilities and fitted lifetimes, and (b) diffusion lengths as a function of SnF₂ fraction, u .

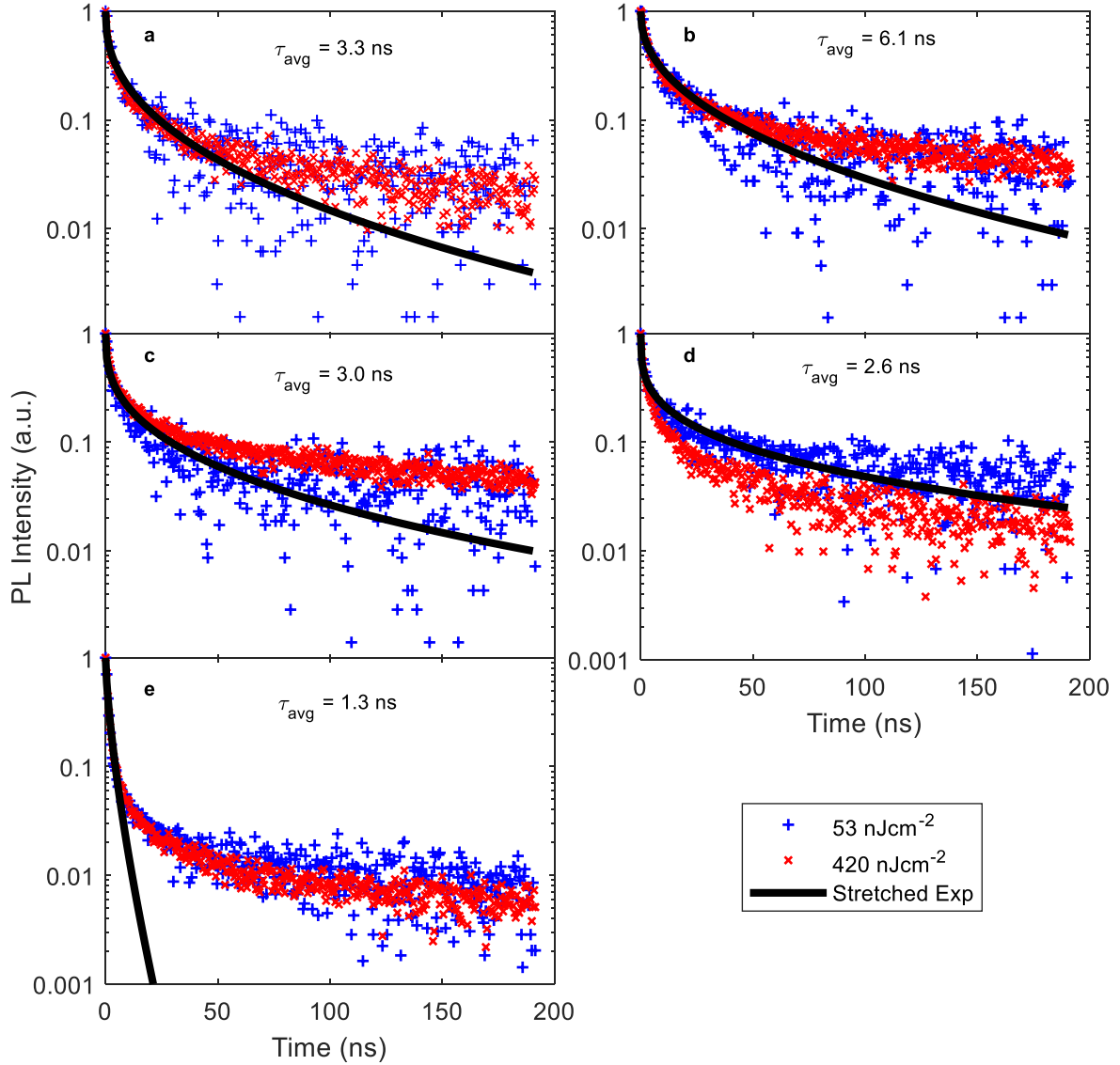


Figure S17. Time-resolved PL data and fits measured using time-correlated single photon counting for different SnF₂ fractions, u : (a) $u=0$, (b) $u=0.027$, (c) $u=0.273$, (d) $u=0.545$, and (e) $u=1$. Photoexcitation was provided by a 400 nm pulsed laser at a repetition rate of 5 MHz. Fluences are given in the legend.

S7. SPECTRAL MISMATCH FACTOR CALCULATIONS

In our laboratory at the University of Oxford, we have two solar simulators for solar cell characterisation that are re-calibrated periodically. One is an ABET Technologies Sun 2000, which uses a conventional filtered Xe lamp, and the other is a Wavelabs Sinus-220, which uses an array of light-emitting diodes (LEDs). In contrast to the LED simulator, the filtered Xe lamp requires particular care in its calibration for low-bandgap solar cells because its spectral irradiance in the near-infrared (NIR) region contains several strong peaks from the Xe spectrum that are not present in the

reference AM1.5G solar spectrum. In other words, the spectral mismatch factor for cells with bandgaps below 1.5 eV can vary significantly compared to cells with larger bandgaps.

In brief, the intensity of the ABET solar simulator is set using a certified reference diode and a measurement of the spectral mismatch factor. A more detailed description of the procedure can be found elsewhere.⁵ Firstly, the solar simulator intensity is set so that a certified Si reference solar cell sitting in the same position as the measurement cells, produces the equivalent J_{SC} as its AM1.5G certified value. Then the spectrum of the lamp is measured with a calibrated spectrograph. The spectra used for characterising solar cells in this work are shown in Figure S18. Subsequently, the spectral mismatch factor for the solar simulator lamp and a representative FACsPbSnI₃ solar cell is calculated. If the mismatch factor is small, the lamp intensity is adjusted to produce a J_{SC} from the Si reference cell that would be expected to provide 100 mW/cm² in the FACsPbSnI₃ cell to account for the spectral mismatch. This is valid for small intensity adjustments so that the shape of the irradiance spectrum remains constant. If large adjustments are required, the spectrum is re-measured so an updated mismatch factor can be calculated and applied. This procedure for calibration is repeated approximately every month. For a finer intensity measurement for each experiment, a secondary photodiode is used that is permanently mounted to the sample stage. Its current is noted at the beginning of each experiment and its relative value with respect to the value measured during the master spectral calibration is used as a scaling factor for the experiment intensity. This value is usually within +/- 2% of the master calibration.

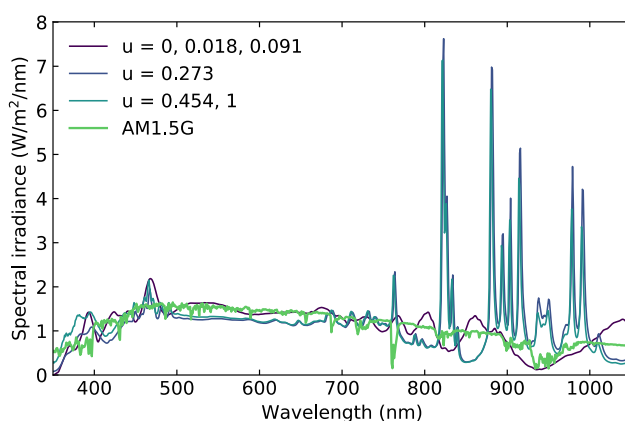


Figure S18. Solar simulator spectral irradiances used for measurements in this work compared to AM1.5G. The values of the SnF₂ fraction, u , in the legend correspond to device variations measured under those spectra.

In this work, the shapes of the external quantum efficiency spectra varied with SnF₂ content in the precursor and were shifted with respect to the reference FACsPbSnI₃ spectrum used in the calibration procedure described above. This means that cells with different compositions measured under the same or very similar spectra have different spectral mismatch factors, and hence are effectively irradiated at different intensities. To correct for this, the spectral mismatch factor

calculation was repeated on the cells in this work to determine how much the lamp intensity should have been adjusted to provide 100 mW/cm^2 . The effective mismatch factor is thus the ratio of the mismatch factor that should have been applied to that which was actually applied, and the effective intensity is the local intensity measured on the sample stage photodiode in number of suns divided by the effective mismatch factor. This additional effective mismatch correction wasn't necessary for the LED simulator, which was already well matched to the solar spectrum regardless of the EQE spectrum. The values for effective mismatch factors and intensities are summarised in Table S3.

S8. SOLAR CELL CHARACTERISATION

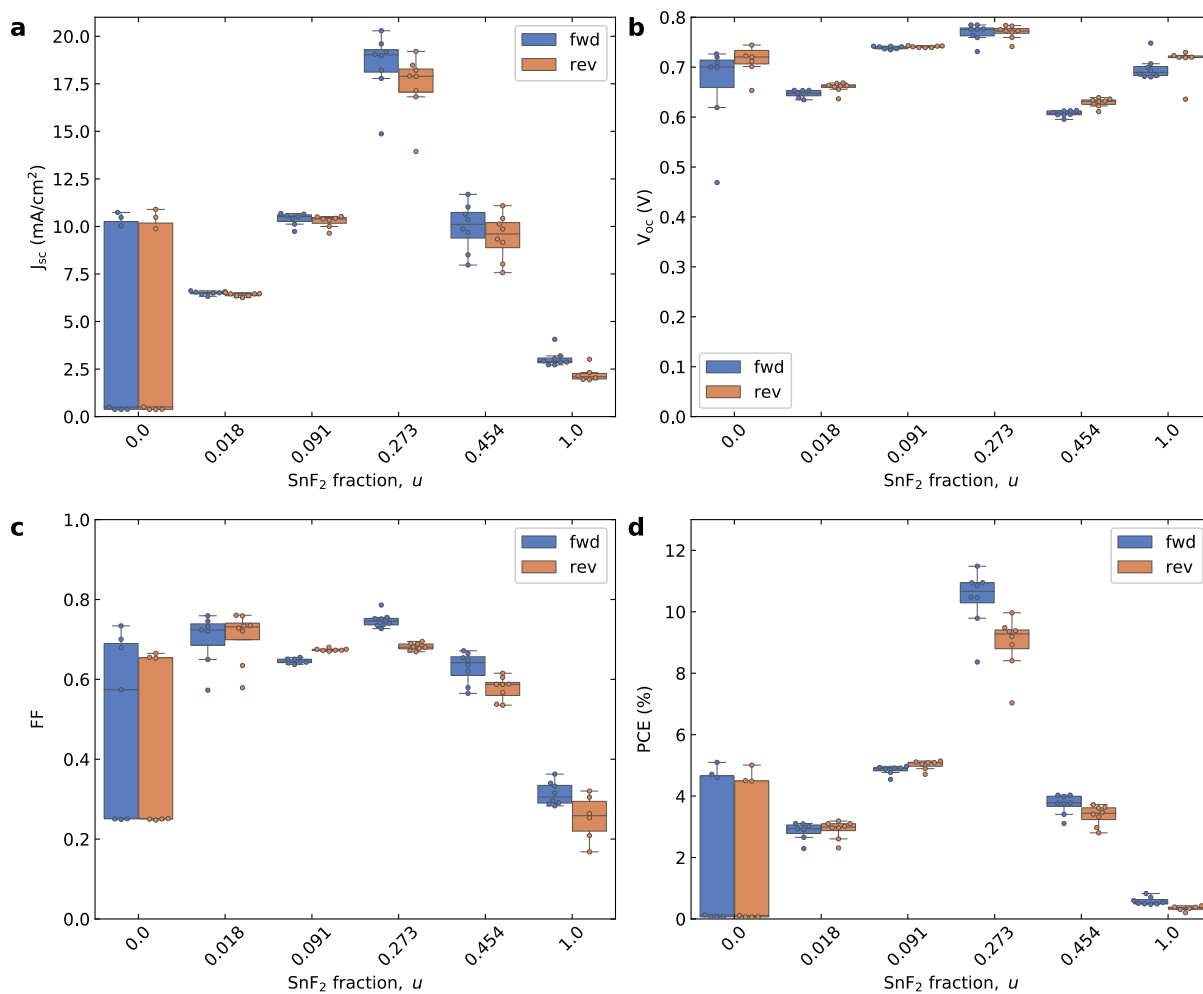


Figure S19. Statistics for device performance parameters made with different SnF₂ fractions, u .

Table S3. Summary of champion cell scanned performance parameters and measurement conditions.

u	J _{sc} (mA/cm ²)	V _{oc} (V)	FF	M	Eff. Irradiance (mW/cm ²)	PCE (%)	Expected J _{sc} under AM1.5G (mA/cm ²)
0	10.48	0.72	0.70	0.98	104	5.10	10.11
0.018	6.51	0.66	0.76	0.99	103	3.19	6.32
0.091	10.52	0.74	0.67	0.99	102	5.14	10.29
0.273	20.29	0.78	0.74	0.98	102	11.48	19.86
0.454	11.69	0.60	0.58	0.98	102	4.03	11.51
1	4.06	0.75	0.32	0.86	116	0.83	3.51

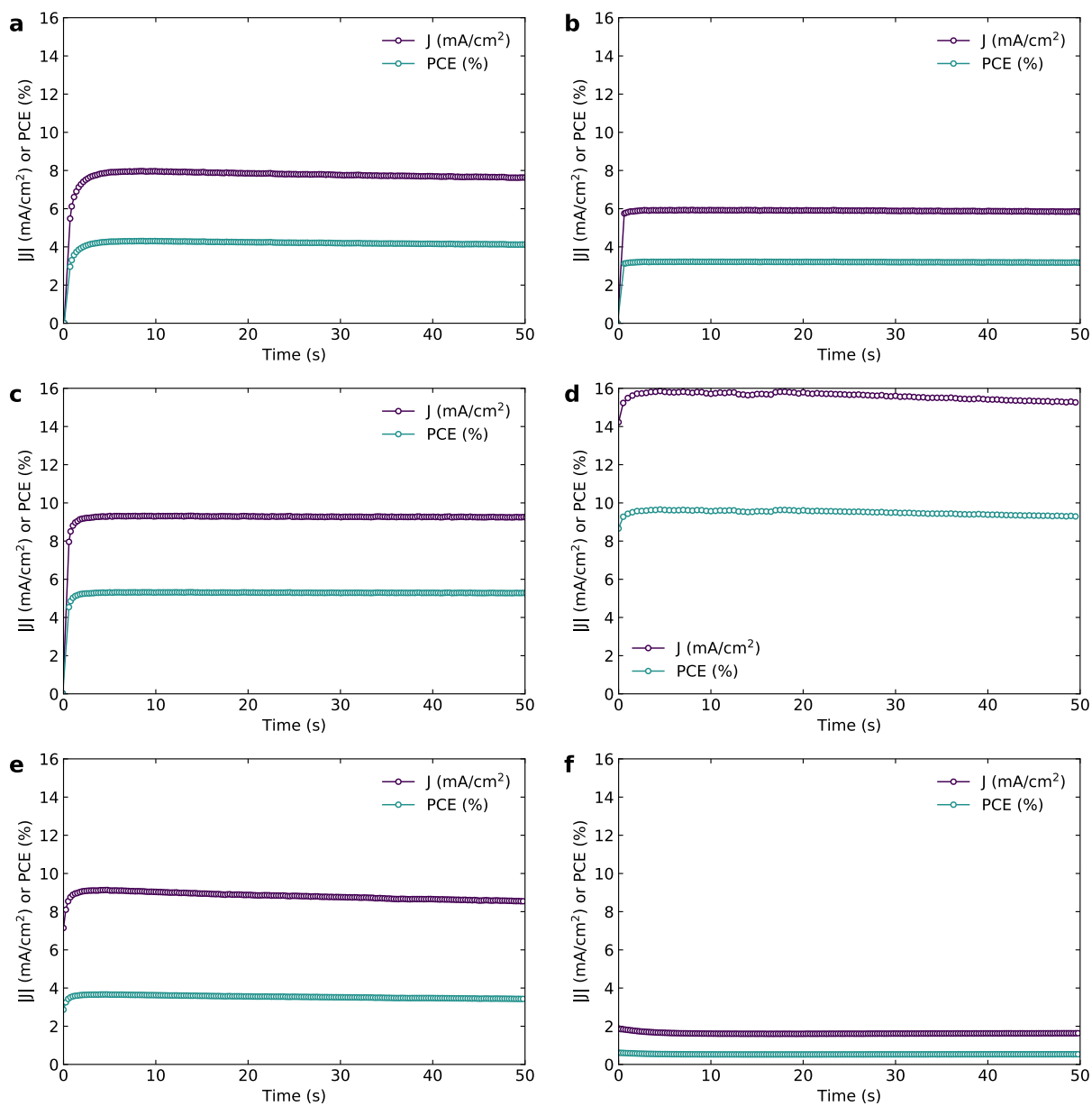


Figure S20. Steady-state current-density and power conversion efficiency at a constant voltage for champion devices of each variation of the SnF_2 fraction, u . (a) $u=0$, (b) $u=0.018$, (c) $u=0.091$, (d) $u=0.273$, (e) $u=0.454$, and (f) $u=1$.

Table S4. Summary of steady-state power output measurements: V_{ss} is the steady-state voltage, J_{50} and PCE_{50} are the current density and power conversion efficiency after 50 s, respectively.

u	V_{ss} (V)	$ J_{50} $ (mA/cm ²)	PCE_{50} (%)
0	-0.56	7.62	4.12
0.018	-0.56	5.84	3.17
0.091	-0.58	9.25	5.28
0.273	-0.62	15.26	9.29
0.454	-0.41	8.55	3.43
1	-0.38	1.63	0.53

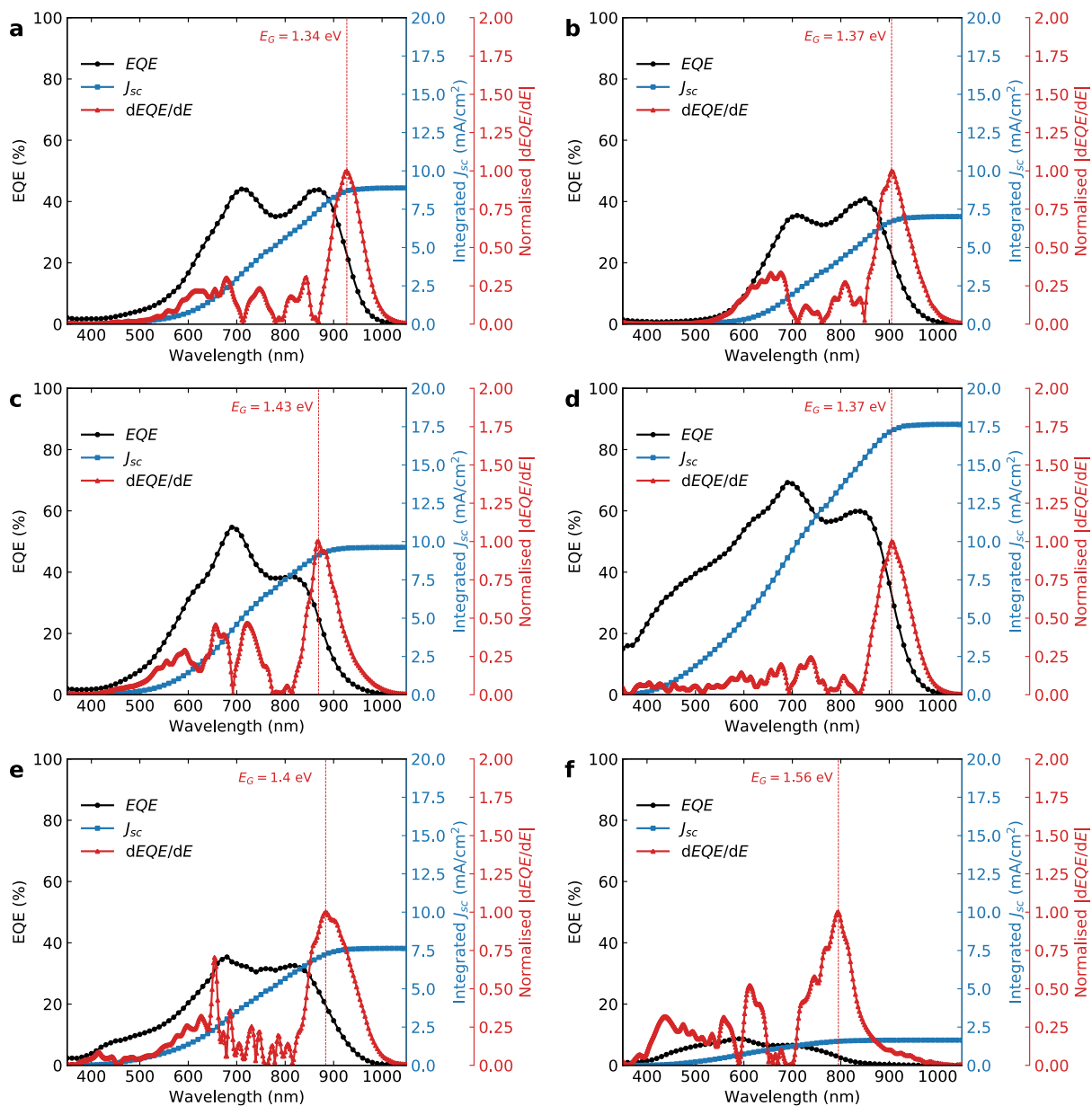


Figure S21. External quantum efficiency, integrated J_{sc} , and normalised $dEQE/dE$ spectra for representative devices for different values of the SnF_2 fraction, u . (a) $u=0$, (b) $u=0.018$, (c) $u=0.091$, (d) $u=0.273$, (e) $u=0.454$, and (f) $u=1$.

S9. THICKNESS MEASUREMENTS

Table S5. Summary of film thickness (d) measurements. The stated errors are the sample standard error based on 5 measurements in different spots of the sample.

u	d (nm)
0	435.2 ± 7.9
0.027	410.8 ± 10.8
0.273	456.4 ± 10.0
0.545	496.2 ± 11.0
1	264.2 ± 36.2

S10. ESTIMATION OF BANDGAPS AND LIMITING V_{OC}

There are several commonly used methods for estimating the bandgaps of perovskites. We have used the following here to estimate the bandgaps of our dual-source co-evaporated perovskite films: Tauc fitting of the optical absorption coefficient (α) as shown in Figure S22 and summarised in Table S6,⁶ Elliot fitting of α as shown in Figure S23 and summarised in Table S7,^{7,8} using the PL peak shown in Figure 3 and summarised in Table S6,⁹ and using the peak of $dEQE/dE$ as shown in Figure S21 and summarised in Table S8.¹⁰ Only films that exhibited a pronounced absorption edge near the expected perovskite bandgap were used for Tauc and Elliot fitting.

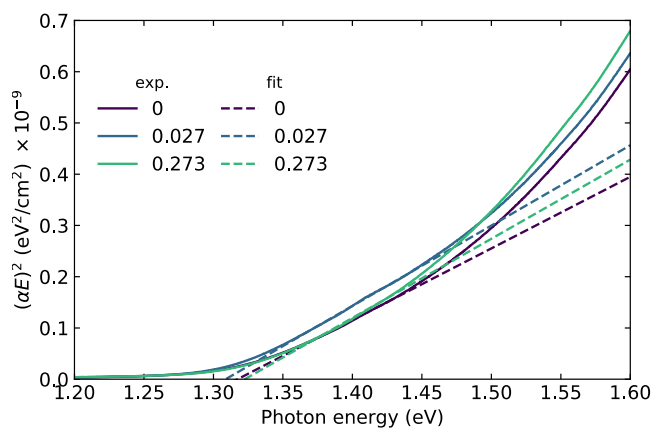


Figure S22. Attempts at Tauc fits to experimental data around the absorption edge of perovskite thin-films. The legend indicates values of the SnF_2 fraction, u .

Table S6. Summary of indicators of perovskite bandgaps based on optical measurements as a function of u .

u	Tauc E_G (eV)	PL Peak (eV)
0	1.32	1.36
0.027	1.31	1.35
0.273	1.32	1.37
0.545	-	1.42
1	-	1.59

Elliot's model^{7,8} for α at the absorption onset in a semiconductor is given by:

$$\alpha = \frac{\alpha_0}{E} \left[\sum_{n=1}^{\infty} \frac{4\pi E_b^{3/2}}{n^3} \delta \left(E - \left(E_G - \frac{E_b}{n^2} \right) \right) + \frac{2\pi\Delta}{1 - \exp(-2\pi\Delta)} \frac{g(E)}{c_0} \right]$$

where α_0 is the absorption coefficient prefactor, E is the photon energy, E_b is the exciton binding energy, n is the order of the exciton transition line, δ is the Dirac delta function, E_G is the bandgap energy, c_0 is the density of states prefactor, Δ is an energy scaling such that $\Delta = \sqrt{E_b/(E - E_G)}$, and $g(E)$ is the density of states given by:

$$g(E) = c_0 \frac{1}{1 - b(E - E_G)} \sqrt{E - E_G}$$

where b is the band non-parabolicity factor. Spectral broadening is accounted for by convolution with the following broadening function:⁸

$$Br(E) = \frac{1}{\cosh\left(\frac{E - E'}{\Gamma}\right)}$$

such that the broadened coefficient is given by:

$$\alpha_{Br} = \alpha * Br(E)$$

The broadened coefficient function, α_{Br} , was fitted to the experimental absorption coefficient data, as shown in Figure S23, to obtain values for E_G , E_b , b , α_0 , and Γ , which are summarised in Table S7. The fitting range was restricted to $1.2 \leq E \leq 1.6$ eV and a constant offset was added (offset = $\alpha(E=1.2 \text{ eV})$) to account for the fact that the absorption coefficient doesn't fall to zero, presumably due to scattering.

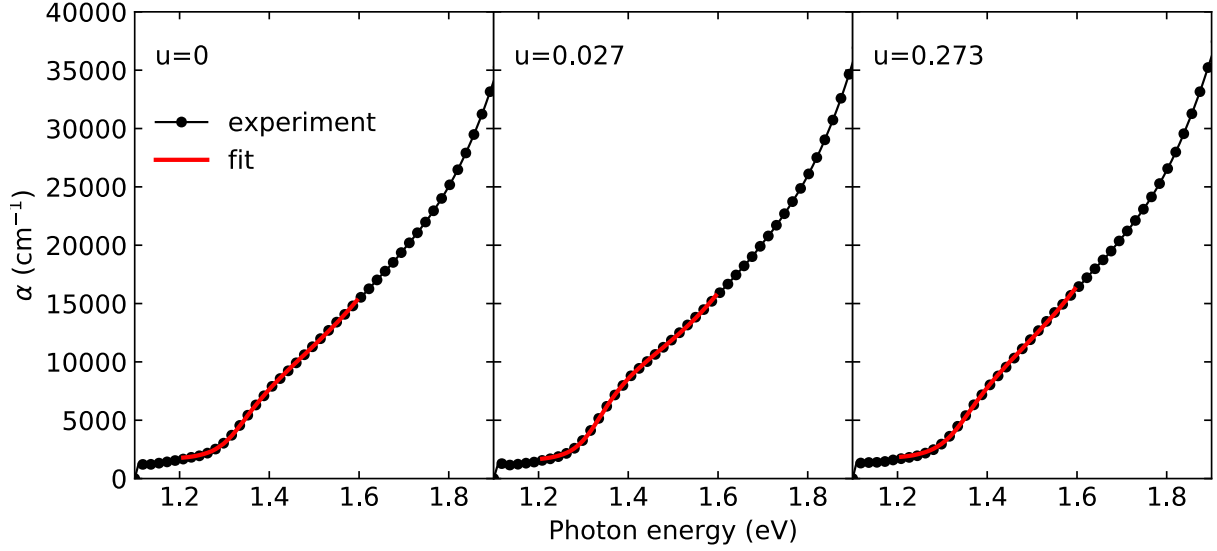


Figure S23. Elliot model fits to the absorption edge in perovskite films for different values of the SnF₂ fraction, u . The markers on the experimental curves indicate every 2nd data point.

Table S7. Summary of fitting parameters for Elliot's model.

u	E_G (eV)	E_b (meV)	b	α_0 (cm ⁻¹)	Γ (meV)
0	1.33	1.08	1.45	2.13×10^4	37.9
0.027	1.34	7.27	1.61	1.62×10^4	36.1
0.273	1.35	1.94	1.51	2.21×10^4	42.6

The limiting photovoltaic performance parameters are usually estimated within the detailed balance formalism.¹¹ This approach assumes the unrealistic case of a step function external quantum efficiency (EQE) spectrum that transitions from 0 to 1 at the bandgap energy. This yields an expression for the open-circuit voltage (V_{oc}) in the Shockley-Queisser (SQ) limit given by:

$$V_{OC,SQ} = \frac{kT}{q} \ln \left(\frac{\int_0^\infty \theta(\lambda_{EG} - \lambda) \phi_{AM1.5G}(\lambda) d\lambda}{\int_0^\infty \theta(\lambda_{EG} - \lambda) \phi_{BB,T=300K}(\lambda) d\lambda} \right) \quad (SX)$$

where k is Boltzmann's constant, T is temperature, q is the charge of an electron, λ is the incident photon wavelength, λ_{EG} is the bandgap wavelength, θ is the Heaviside step function, and ϕ is the incident photon flux for either solar illumination (AM1.5G) or a black-body at 300K (BB,T=300K). As mentioned above, there are several methods of estimating the appropriate bandgap for this calculation. Using the values obtained from optical measurements of bare thin-films may be appropriate for estimating the intrinsic absorber bandgap but unrealistic for estimating limiting photovoltaic device parameters because real solar cells have EQE spectra that are not step functions, i.e. they do not exhibit a sharp cut-off at the bandgap energy. One approach to counteract this effect is to represent the measured spectra by a distribution of step functions, which is given by the derivative

of the EQE spectrum with respect to energy, $dEQE/dE$.¹⁰ The peak of this distribution can be taken as the effective bandgap energy used to calculate device parameters in the SQ limit.

Additionally, there is a loss in V_{OC} due to incomplete light absorption and carrier collection leading to a reduction in J_{SC} . Accounting for this by using the measured EQE spectra, the limiting V_{OC} for a given device can be expressed as:

$$V_{OC,rad} = \frac{kT}{q} \ln \left(\frac{\int_0^\infty EQE(\lambda) \phi_{AM1.5G}(\lambda) d\lambda}{\int_0^\infty EQE(\lambda) \phi_{BB,T=300K}(\lambda) d\lambda} \right) \quad (SX)$$

Further losses in the V_{OC} also come from non-radiative recombination. The expected external electroluminescence quantum yield (η_{EL}) for a solar cell can therefore be estimated based on the limiting and measured V_{OC} 's (assuming a diode ideality factor of $n=1$ represents a lower limit):¹⁰

$$\eta_{EL} = \exp \left(- \frac{q}{nkT} (V_{OC,rad} - V_{OC}) \right) \quad (SX)$$

A summary of parameter estimates based on these calculations is given in Table S8.

Table S8. Summary of V_{OC} and electroluminescence quantum yield calculations based on the estimation of the bandgap given by the peak of $dEQE/dE$.

u	Peak $dEQE/dE$ (eV)	$V_{OC,SQ}$ (V)	$V_{OC,rad}$ (V)	$V_{OC,rad}-V_{OC}$ (V)	η_{EL} (%)
0	1.34	1.08	1.02	0.30	8.42×10^{-4}
0.018	1.37	1.11	1.02	0.36	7.60×10^{-5}
0.091	1.43	1.16	1.05	0.31	6.48×10^{-4}
0.273	1.37	1.11	1.05	0.27	3.26×10^{-3}
0.454	1.40	1.14	1.04	0.44	3.71×10^{-6}
1	1.56	1.29	1.09	0.34	2.19×10^{-4}

S11. SOLUTION PROCESSED FILMS AND DEVICES

Solution processed perovskite films were prepared with the same Cs:Sn:Pb ratio in the starting solution as obtained from ICP-MS of the best evaporated composition. SnF_2 was incorporated into the solutions either substitutionally or in excess of the SnI_2 at a ratio of 10 mol%. Solution processed films were prepared by spincoating in a glovebox. Perovskite films for XRD and absorption spectroscopy were prepared on quartz substrates. Perovskite films for devices were prepared in the same device structure with the same processing method as used for devices with evaporated perovskite layers.

The XRD spectra are shown in Figure S24 compared to an evaporated perovskite film made with the composition of the champion device. The lattice parameters determined from these spectra are shown in Table S9. The unit cells of the two solution processed variants are very similar. The

evaporated film has a slightly larger cell volume mainly due to elongation along the c-axis. This could be due to more incorporation of Pb into the lattice. This would imply that the impurity phase would have to be Sn-rich and thus the perovskite layer would contain more Pb than indicated by ICP-MS. Quantification of these effects is the topic of ongoing work.

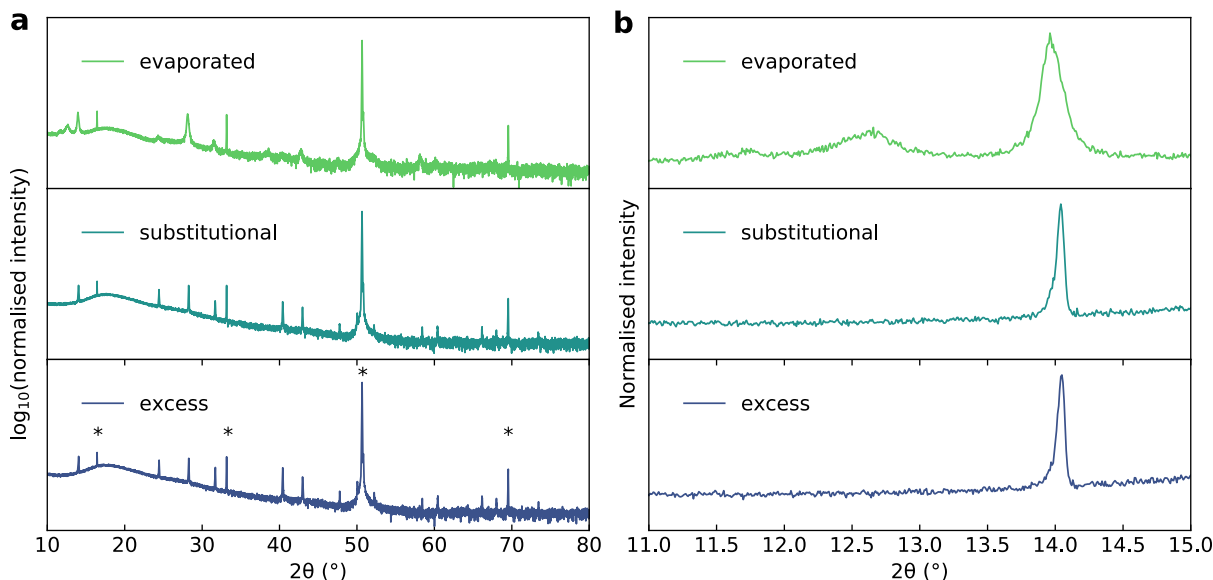


Figure S24. XRD spectra of perovskite films on quartz substrates comparing the best evaporated composition (SnF_2 fraction $u=0.273$) to solution processed films: (a) full measurement range, and (b) comparison in the low angle region. Peaks corresponding to the z-cut quartz substrates are highlighted with asterisks. The 2θ angle corresponds to the $K\alpha_1$ wavelength of the Cu x-ray source.

Table S9. Summary of lattice parameters determined from XRD measurements of solution processed perovskite films, where SnF_2 was incorporated either substitutionally or in excess of SnI_2 , compared to an evaporated film of the best performing composition (SnF_2 fraction $u=0.273$).

Condition	a (Å)	b (Å)	c (Å)	α (°)	β (°)	γ (°)	volume (Å ³)
Evaporated	6.345(3)	8.941(4)	9.044(4)	90	90	90	8.42×10^{-4}
Substitutional	6.3246(7)	8.9320(8)	8.942(4)	90	90	90	7.60×10^{-5}
Excess	6.3259(3)	8.9317(5)	8.939(2)	90	90	90	2.19×10^{-4}

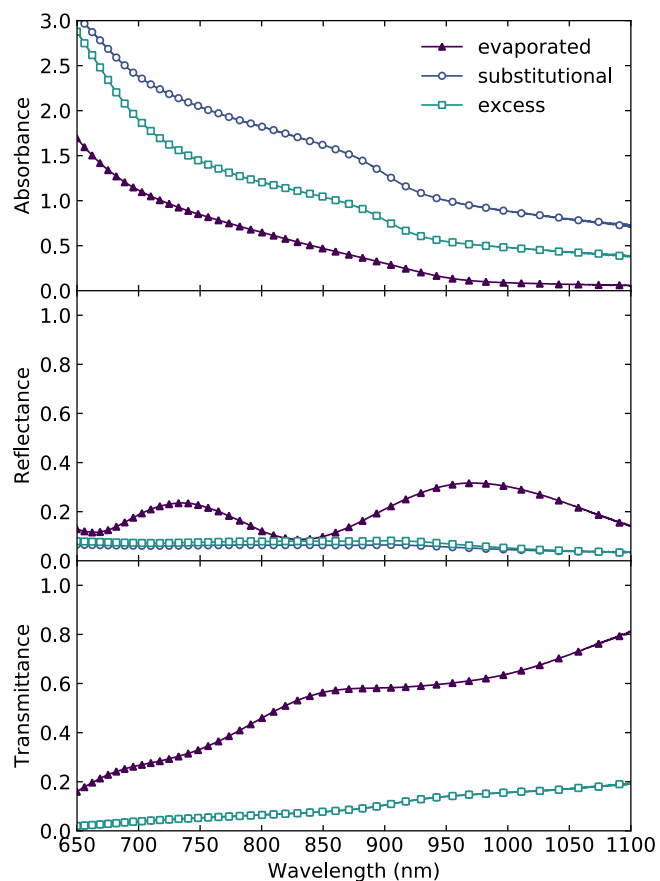


Figure S25. UV-vis-NIR absorbance, reflectance, and transmittance spectra of perovskite films on quartz substrates comparing the best evaporated composition (SnF_2 fraction $u=0.273$) to solution processed films where SnF_2 was incorporated either substitutionally or in excess of SnI_2 . Markers indicate every 75th data point. Absorbance is calculated as $A = -\ln(T/(1 - R))$. The solution processed films scatter significantly more light than the evaporated film as evidenced by their high non-zero absorbance below the band-edge and absence of interference fringes in their reflectance spectra.

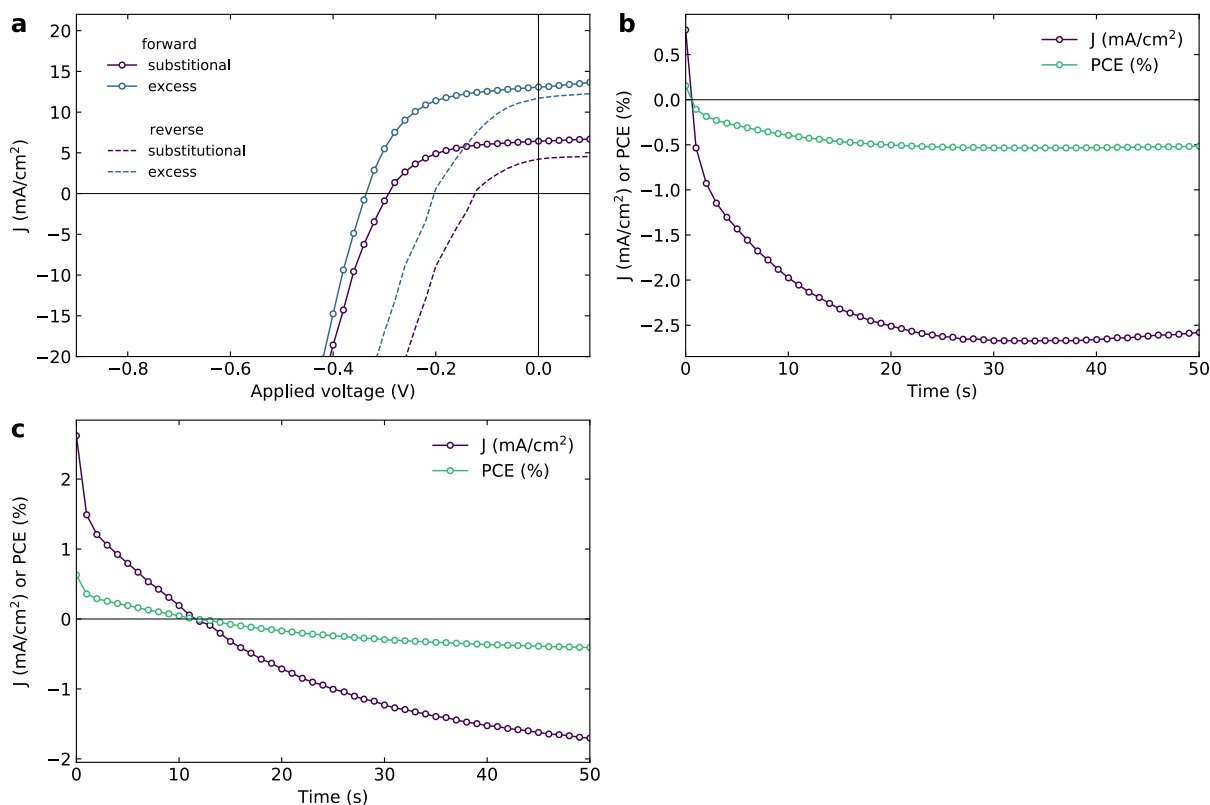


Figure S26. Device characterisation. (a) J-V characteristics of devices where the perovskite layer was solution-processed with the SnF₂ incorporated either substitutionally or in excess to the SnI₂. Solid lines with symbols show the forward scan direction (V_{OC} to J_{SC}) and dashed lines show the reverse scan direction (J_{SC} to V_{OC}). Steady-state current-density and power conversion efficiency at a constant voltage where SnF₂ was incorporated either (b) substitutionally or (c) in excess. Both the PCE and current-density dropped below zero at constant voltage because the devices degraded to a point where the scanned maximum power point fell outside of the power generating quadrant.

Table S10. Summary of device performance parameters from the best J-V scan where the perovskite layer was solution processed and SnF₂ was incorporated either substitutionally or in excess of SnI₂.

Condition	J_{SC} (mA/cm ²)	V_{OC} (V)	FF	PCE (%)
Substitutional	6.43	0.29	0.52	0.96
Excess	13.07	0.34	0.55	2.36

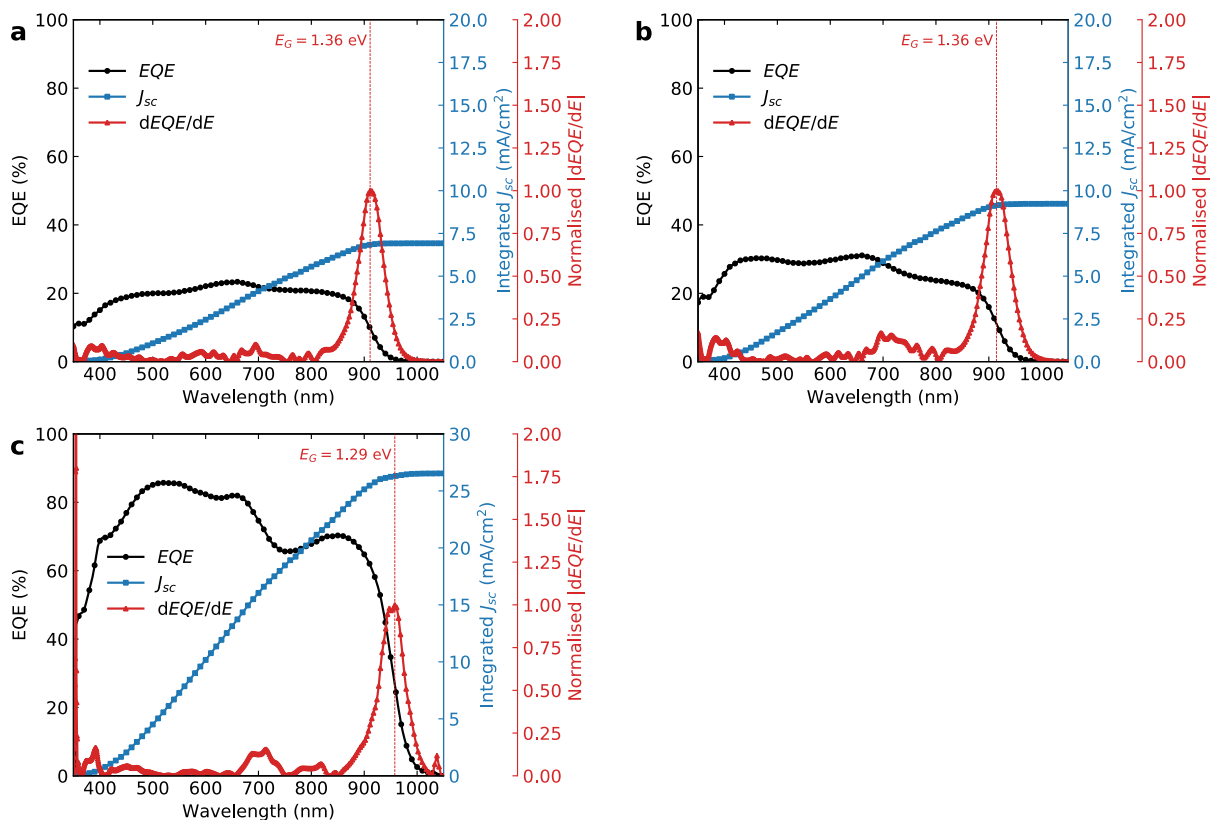


Figure S27. External quantum efficiency, integrated J_{sc} , and normalised $dEQE/dE$ spectra for devices with solution processed perovskite layers where the SnF_2 was incorporated into the solution either (a) substitutionally or (b) in excess of SnI_2 ; (c) EQE spectrum digitised¹² from published data where the Cs:Pb:Sn ratio was 25:50:50 ($\text{FA}_{0.75}\text{Cs}_{0.25}\text{Pb}_{0.5}\text{Sn}_{0.5}\text{I}_3$).⁹ The latter EQE has a red-shifted effective bandgap consistent with the devices studied here containing a high Sn content.

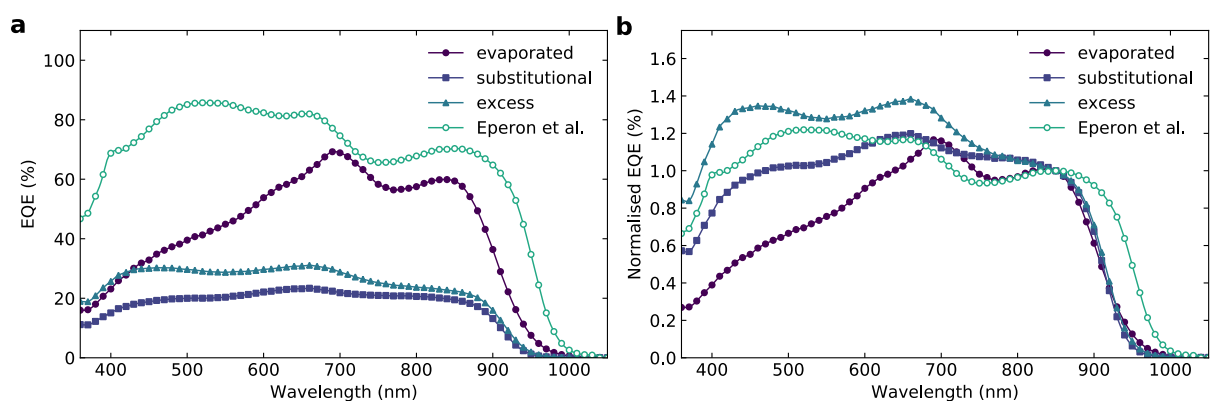


Figure S28. Comparison of EQE spectra between the best evaporated composition in the present work (SnF_2 fraction $u=0.273$), the two solution processed variations (with the same stoichiometry as obtained from ICP-MS measurements, $\text{FA}_{0.98}\text{Cs}_{0.02}\text{Sn}_{0.03}\text{Pb}_{0.97}\text{I}_3$) where SnF_2 was incorporated either substitutionally or in excess of SnI_2 , and published data (digitised)¹² where Cs:Pb:Sn ratio was 25:50:50 ($\text{FA}_{0.75}\text{Cs}_{0.25}\text{Pb}_{0.5}\text{Sn}_{0.5}\text{I}_3$).⁹ (a) Absolute EQE, and (b) EQE normalised at 850 nm.

REFERENCES

1. Schindelin, J. *et al.* Fiji: an open-source platform for biological-image analysis. *Nat. Methods* **9**, 676–682 (2012).
2. Schneider, C. A., Rasband, W. S. & Eliceiri, K. W. NIH Image to ImageJ: 25 years of image analysis. *Nat. Methods* **9**, 671–675 (2012).
3. Joyce, H. J., Boland, J. L., Davies, C. L., Baig, S. A. & Johnston, M. B. A review of the electrical properties of semiconductor nanowires: insights gained from terahertz conductivity spectroscopy. *Semicond. Sci. Technol.* **31**, 103003 (2016).
4. Johnston, M. B. & Herz, L. M. Hybrid Perovskites for Photovoltaics: Charge-Carrier Recombination, Diffusion, and Radiative Efficiencies. *Acc. Chem. Res.* **49**, 146–154 (2016).
5. Snaith, H. J. How should you measure your excitonic solar cells? *Energy Environ. Sci.* **5**, 6513–6520 (2012).
6. Tauc, J. Optical properties and electronic structure of amorphous Ge and Si. *Mater. Res. Bull.* **3**, 37–46 (1968).
7. Elliott, R. J. Intensity of Optical Absorption by Excitons. *Phys. Rev.* **108**, 1384–1389 (1957).
8. Saba, M. *et al.* Correlated electron–hole plasma in organometal perovskites. *Nat. Commun.* **5**, 5049 (2014).
9. Eperon, G. E. *et al.* Perovskite-perovskite tandem photovoltaics with optimized band gaps. *Science* **354**, 861–865 (2016).
10. Rau, U., Blank, B., Müller, T. C. M. & Kirchartz, T. Efficiency Potential of Photovoltaic Materials and Devices Unveiled by Detailed-Balance Analysis. *Phys. Rev. Appl.* **7**, 044016 (2017).
11. Shockley, W. & Queisser, H. J. Detailed Balance Limit of Efficiency of p-n Junction Solar Cells. *J. Appl. Phys.* **32**, 510–519 (1961).
12. Rohatgi, A. WebPlotDigitizer, v4.2. (2019). Available at: <https://automeris.io/WebPlotDigitizer>.